ELSEVIER

The value of multiangle measurements for retrieving structurally and radiatively consistent properties of clouds, aerosols, and surfaces

David J. Diner [a,*], Bobby H. Braswell [b], Roger Davies [a], Nadine Gobron [c], Jiannan Hu [d],
Yufang Jin [e], Ralph A. Kahn [a], Yuri Knyazikhin [d], Norman Loeb [f], Jan-Peter Muller [g],
Anne W. Nolin [h], Bernard Pinty [c], Crystal B. Schaaf [d], Gabriela Seiz [i], Julienne Stroeve [j]

[a]*Jet Propulsion Laboratory, California Institute of Technology, Pasadena, CA, United States*
[b]*University of New Hampshire, Durham, NH, United States*
[c]*Joint Research Centre, Ispra, Italy*
[d]*Boston University, Boston, MA, United States*
[e]*University of California at Irvine, Irvine, CA, United States*
[f]*NASA Langley Research Center, Hampton, VA, United States*
[g]*University College London, London, UK*
[h]*Oregon State University, Corvallis, OR, United States*
[i]*Swiss Federal Institute of Technology (ETH), Zurich, Switzerland*
[j]*University of Colorado, Boulder, CO, United States*

Abstract

Passive optical multiangle observations make possible the retrieval of scene structural characteristics that cannot be obtained with, or require fewer underlying assumptions than, single-angle sensors. Retrievable quantities include aerosol amount over a wide variety of surfaces (including bright targets); aerosol microphysical properties such as particle shape; geometrically-derived cloud-top heights and 3-D cloud morphologies; distinctions between polar clouds and ice; and textural measures of sea ice, ice sheets, and vegetation. At the same time, multiangle data are necessary for accurate retrievals of radiative quantities such as surface and top-of-atmosphere albedos, whose magnitudes are governed by structural characteristics of the reflecting media and which involve angular integration over intrinsically anisotropic intensity fields. Measurements of directional radiation streams also provide independent checks on model assumptions conventionally used in satellite retrievals, such as the application of 1-D radiative transfer theory, and provide data required to constrain more sophisticated, 3-D approaches. In this paper, the value of multiangle remote sensing in establishing physical correspondence and self-consistency between scene structural and radiative characteristics is demonstrated using simultaneous observations from instruments aboard NASA's Terra satellite (MISR, CERES, ASTER, and MODIS). Illustrations pertaining to the remote sensing of clouds, aerosols, ice, and vegetation properties are presented.
© 2005 Elsevier Inc. All rights reserved.

Keywords: Multiangle remote sensing; Terra; MISR; CERES; ASTER; MODIS

1. Introduction

Solar radiation is the fundamental energy source for the Earth's climate system and its web of life. Aerosols having a host of sizes, shapes, and atmospheric distributions absorb and scatter radiation over different surface types, resulting in a range of regional climate influences. Stratiform and cumuliform cloud fields with various spatial distributions of water and ice exist throughout the atmosphere's vertical domain, cooling or heating the surface below. These surfaces in turn–smooth and crevassed, forested and arid, rural and urban–influence and are transformed by atmospheric, geodynamic, and biological processes. The complexity of the Earth system makes diagnosis and prediction of

climatic, environmental, and ecological changes enormously challenging. Among the technologies that can be brought to bear upon this challenge, satellites offer the most effective means of measuring patterns and evaluating the performance of models on the global scale. The interaction of sunlight with chemical components of the Earth system yield myriad distributions of spectral reflectance; the morphology, vertical stratification, geometric orientation, and roughness of reflecting elements also give rise to microscopic and macroscopic patterns of angular reflectance that provide structural clues and information on the spatial partitioning of radiation among vertical layers.

Multiangle observations bridge atmospheric and surface 3-D physical structure, the anisotropy of radiant energy, and hemispherically integrated radiative flux. Attaining this cohesion between internal physical properties and external radiation anisotropy is a prerequisite to obtaining self-consistent models of Earth system processes. Such a strategy, as opposed to ones that "tune" certain variables to generate the right radiation intensity or cloud, aerosol, or surface cover amount, or one that presumes self-consistency without verifying underlying assumptions, is the only way that models can be used with confidence to predict the Earth system's responses to future perturbations. In this paper, we show how measurements of reflection anisotropy are diagnostic of structural properties of hazy, cloudy, ice-covered, and vegetated scenes on the one hand, and constrain fundamental radiation parameters that integrate over angle, like top-of-atmosphere albedo, surface albedo, or fraction of absorbed photosynthetically active radiation on the other. We illustrate this correspondence using data from NASA's Terra satellite, which provides multiangle views from several onboard instruments. Terra data contribute to three broad areas of research: How do different cloud types affect and respond to climate variations? What are the climatic and environmental impacts of airborne particulates (aerosols)? How does the surface respond to climate and environmental change? Multiangle information has been proposed as a key player in each of these areas (Diner et al., 1999; Liang et al., 2000); several years of Terra data now afford a refined view of some unique contributions of such measurements. In this paper, we illustrate how such data make fundamental contributions toward self-consistent, physical models of radiatively important elements of the Earth system.

2. Data sources

The interpretation of multiangle information can be categorized into two main strategies: radiometric and geometric. The first refers to changes in the brightness, color, contrast, or other radiance-related quantities as a function of view angle, captured at optical wavelengths by quantities such as the Bidirectional Reflectance Distribution Function (BRDF) (Martonchik et al., 2000; Nicodemus et

al., 1977), which is governed by the composition, density, and geometric structure of the reflecting medium and exemplified through glints, shadows, and volumetric scattering. The second involves real or apparent differences in the shape or location of observed objects, resulting from changes in perspective (for targets with 3-D structure), stereoscopic parallax (displacement dependent upon distance from the observer), or actual motion of the target during the time interval between views.

In an earlier paper (Diner et al., 1999), we distinguished between a "simultaneous" multiangle observing strategy, in which measurements at more than one angle in an orientation along the flight direction are acquired within a period of several minutes, and a "sequential" strategy whereby data from wide-field-of-view cross-track scanners are composited over many days or weeks. Instruments that acquire simultaneous multiangle data include the Along-Track Scanning Radiometer (ATSR) and its successors ATSR-2 and AATSR (Koelemeijer et al., 1998; Stricker et al., 1995), the Polarization and Directionality of the Earth's Reflectances (POLDER-1 and its successors) (Deschamps et al., 1994; Hautecoeur & Leroy, 1998), the Multi-angle Imaging SpectroRadiometer (MISR) (Diner et al., 1998, 2002), and the Advanced Spaceborne Thermal Emission and Reflectance radiometer (ASTER) (Abrams, 2000; Yamaguchi et al., 1998). The sequential strategy is used with MODerate-resolution Imaging Spectroradiometer (MODIS) for certain applications (Lucht et al., 2000; Schaaf et al., 2002; Wanner et al., 1997). Combinations of simultaneous and sequential observing are obtained by the Clouds and the Earth's Radiant Energy System (CERES) scanners (Wielicki et al., 1995). For scenes in which atmospheric or surface temporal variations are minimal, or for which multiangle signatures of a statistical nature are sufficient, the sequential strategy can be effective. However, for dynamically varying targets for which multiangle information is to be used for instantaneous scene characterization, identification, or classification purposes, the simultaneous strategy is required.

NASA's Terra spacecraft was launched into polar, 10:30 am equator-crossing sun-synchronous orbit on 18 December 1999. MISR, ASTER, MODIS, and CERES are four of the five science instruments aboard Terra. Their principal observational attributes are summarized in Table 1. Each uses multiangle measurements to a greater or lesser degree (the fifth instrument, Measurements of Pollution in the Troposphere-MOPITT-which retrieves atmospheric carbon monoxide concentration, does not employ a multiangle strategy):

- MISR observes the Earth in reflected sunlight at nine different view zenith angles and four spectral bands. In its global science mode, ground spatial sampling is 275 m for all nadir bands and the off-nadir red channels, and 1.1 km for the remainder. It takes 7 min for a point to be observed at all nine angles as the spacecraft flies overhead.

Table 1
Attributes of Terra instruments with multiangle capability

	MISR	CERES	ASTER	MODIS
Description	Multiangle pushbroom imager	Scanners	Multispectral imager	Whisk-broom imaging scanner
Angular coverage	0°, 26°, 46°, 60°, 70°, forward and backward of nadir	Limb to limb	Nadir, 31° backward of nadir	0–55° continuously (cross-track)
Multiangle strategies employed	Radiometric, geometric	Radiometric	Geometric	Radiometric
Spectral coverage	446, 558, 672, and 866 nm	Shortwave: 0.3–5 μm Thermal "window": 8–12 μm Total: 0.3–200 μm	Visible/near infrared (VNIR): 3 bands (only the NIR band is stereo) Shortwave infrared (SWIR): 6 bands Thermal infrared (TIR): 5 bands	36 bands between 0.4 and 14.5 μm
Spatial resolution	275 m or 1.1 km, depending on channel	20 km (at nadir)	VNIR: 15 m SWIR: 30 m TIR: 90 m	250 m–1 km (at nadir), depending on channel
Scene dimensions	Pole-to-pole × 400 km	Pole-to-pole × limb-to-limb	60 km × 60 km	Pole-to-pole × 2300 km
Global coverage time	9 days	1 day	NA	2 days

- CERES operates in four scan modes: cross-track, along-track, rotating azimuth plane (RAP), and programmable azimuth plane (PAP). The cross-track scan optimizes spatial sampling but has limited angular sampling; the along-track scan provides measurements near the satellite orbital plane at several view zenith angles with near-simultaneity over the same region; the RAP mode scans in view zenith angle as it rotates in azimuth; and the PAP is used for specific experiments (e.g., field campaigns and intercalibration with other instruments).
- ASTER's Visible and Near Infrared (VNIR) subsystem includes both a nadir view and an additional backward telescope for stereo, with a spatial resolution of 15 m. There is a time lag of about 55 s between the nadir and backward views.
- MODIS only acquires one look per overpass, but obtains multiangle information using the sequential strategy over a 16-day period (the repeat cycle of the Terra orbit), capitalizing on its broad swath. Since MODIS scans cross-track, whereas MISR's view angles are arrayed along-track, the angular samples from these instruments are complementary.

3. Multiangle structural and radiative characterizations

3.1. Clouds

3.1.1. Background

Clouds play a critical role in climate because of their influence on the Earth's energy and hydrological cycles. Due to their complexity, clouds are also responsible for major uncertainties in climate model predictions of the Earth's response to forced perturbations, such as enhanced greenhouse gas abundances. Even small changes in the global distribution of cloud properties can match the 4 W m^{-2} forcing associated with a doubling of the atmospheric carbon dioxide concentration. A useful measure of the effect of clouds on the Earth's radiation budget is "cloud radiative forcing" (CRF), defined as the difference between the radiative flux density under cloud-free and all-sky conditions. The magnitude and sign of this forcing depends on cloud radiative properties and brightness of the underlying surface. In order to improve our understanding of how cloud properties may change in response to an evolving climate and how such changes feed back upon the climate system, it is important to accurately measure CRF as a function of the major cloud types.

3.1.2. Value of multiangle data

Converting directionally-sampled radiances to radiative flux requires angular distribution models (ADMs) that account for the anisotropy of Earth scenes. The first global estimates of CRF were made during the Earth Radiation Budget Experiment (ERBE) (Barkstrom, 1984; Harrison et al., 1990; Ramanathan et al., 1989) using ADMs developed for 12 scene types (Suttles et al., 1988, 1989). Owing to the limited accuracy of the ERBE ADMs, however, errors in both shortwave (SW) and longwave (LW) radiative fluxes were found to depend strongly on cloud properties (Loeb et al., 2003b), thereby limiting their applicability for determining CRF by cloud type.

Using multiangle measurements from CERES, coincident imager retrievals of cloud and aerosol data (e.g., from MODIS), and meteorological information from data assimilation models, new ADMs have recently been developed that dramatically improve the accuracy of both SW and LW TOA radiative fluxes compared to ERBE (Loeb et al., 2003a,b, 2005; also see http://asd-www.larc.nasa.gov/Inversion/ for figures and tabulations of the ADMs). In the shortwave, CERES TOA flux errors are a factor of 2–5 smaller than ERBE, with the largest improvements occurring for thin ice clouds and thick liquid water clouds. In the longwave, CERES flux errors

are typically a factor of 1.5–2 smaller than ERBE, with the largest reduction in error occurring for thin and moderately thick ice clouds. Comparisons of the improved CERES ADMs with climate model results are now beginning to occur (e.g., Xu et al., in press).

With the advent of automated, global stereo cloud height retrievals from MISR to complement and improve upon simpler threshold-based infrared imager cloud height measurements, additional improvements in relating CRF to cloud type are underway. Multiangle imagery from a sensor like MISR makes it possible to capture cloud-top heights (CTH), the morphological structure of vertically developed clouds, and cloud advection velocities as a result of the time difference between the various looks (Horváth & Davies, 2001; Moroney et al., 2002; Muller et al., 2002; Zong et al., 2002) based on a purely stereophotogrammetric (i.e., geometric) retrieval approach. Validation using ground-based 35/94 GHz radar and lidar retrievals of single-layer clouds shows instantaneous accuracies typically within the predicted height resolution (~560 m) of MISR's operational Multipoint Matcher algorithm (Muller et al., 2002; Naud et al., 2002, 2004, in press). A case study comparing automated MISR CTH retrievals with high

spatial resolution stereo from ASTER is shown in Fig. 1. The top portion shows coincident ASTER and MISR cloud imagery over Zurich-Kloten, Switzerland on 12 April 2002. The bottom panels include height histograms extracted using the Multi-Photo Geometrically Constrained Least-Squares Matching (MPGC LSM) algorithm (Baltsavias, 1991; Gruen, 1985), a computationally intensive method known for its high accuracy and reliability. Stereo CTHs with an accuracy of ±12.5 m and ±280 m can be retrieved with this algorithm from ASTER and from MISR's nadir and near-nadir (26°) cameras, respectively, independent of the actual cloud height and wind speed (Seiz, 2003; Seiz et al., submitted for publication). The MISR operational product shows good agreement with these more computationally intensive retrievals. Additional MISR-ASTER matchups were acquired during the December 2004 Rain in Cumulus over Ocean (RICO) campaign, and are in the process of being analyzed.

A key characteristic of MISR stereo heights is that the measurements are insensitive to atmospheric temperature profile, emissivity, and radiometric calibration drifts, thereby providing weather and climate diagnostics independent of common error sources and making possible the
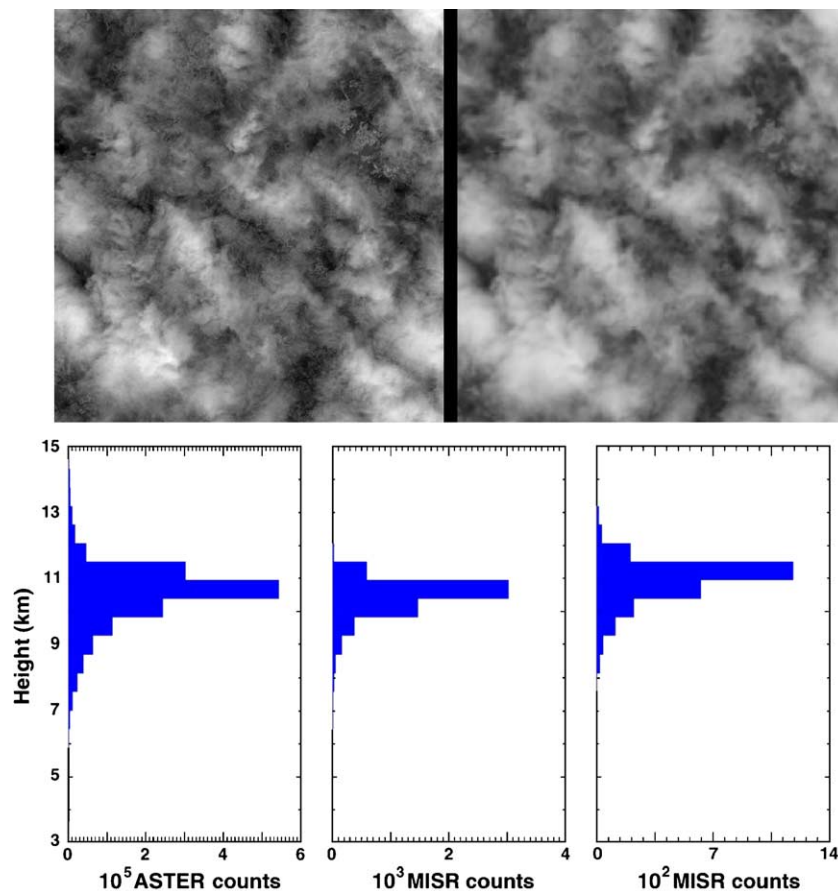

Fig. 1. Top: ASTER (left) and MISR imagery (right) on 12 April 2002 over Zurich-Kloten, Switzerland (Terra orbit 12321). The area of the scene is approximately 60 × 60 km. Bottom: CTH histograms from ASTER, using the MPGC LSM matcher (left); from MISR, using the MPGC LSM matcher (center); and from MISR using the computationally faster Multipoint Matcher used in standard processing (right). The spatial resolution of the CTH grid is 15 m (ASTER), 275 m (MISR MPGC LSM) and 1100 m (MISR L2TC), respectively. No cloud motion correction was applied to these data.

accurate determination of temporal trends. Using statistical averaging to reduce instantaneous retrieval errors, a preliminary analysis by Davies and Moroney (2005) indicates a sensitivity of approximately ±10 m in the global, annual difference in effective CTH between one year and another. The analysis to date implies that the annually averaged effective CTH in 2004 was 40 m lower that in 2000, primarily due to a reduction in high-cloud fraction. The climate significance of this initial result must await an examination of the intervening and subsequent years, which will occur once the MISR data are reprocessed with the same pedigree of geometric calibration. Nonetheless, this capability is notable in light of a multiagency report on climate observing requirements (Ohring et al., 2004), which derived a decadal cloud height stability requirement of 30 m in order to detect variation attributable to climate change. The report also calls for "independent instrument measurements from space of each key climate variable" as a means of verifying the accuracy of subtle climate-related effects. As a consequence of their unique observational attributes, the geometrically-derived global CTHs from MISR satisfy this requirement, underscoring the importance of continued acquisition of such diagnostics beyond the lifetime of Terra in order to establish linkages between any observed trends and the temporal nature of climate forcings.

Using MISR and MODIS to characterize the cloud cover and cloud height distribution in $1° \times 1°$ regions observed by CERES in its along-track scan mode, SW CRF as a function of cloud type for 12 April 2000 is shown in Fig. 2. Each $1° \times 1°$ region is sorted according to total cloud cover into partly (0.1–40%), mostly (40–99.9%), and overcast (>99.9%) cloud classes, and according to cloud height for single-layer low (0–2 km), single-layer middle (2–6 km), single-layer high (>6 km), and multilayer cloud classes. Next, the frequency distribution of SW CRF from CERES for footprints falling in $1° \times 1°$ regions that are partly cloudy (Fig. 2a), mostly cloudy (Fig. 2b), overcast (Fig. 2c), and for all cloud conditions (Fig. 2d) is determined for each cloud height class. To estimate SW CRF for a CERES footprint, the instantaneous TOA flux is compared with a clear-sky TOA flux from monthly mean SW clear-sky flux maps for April 2000. In Fig. 2 the SW CRF is expressed in (dimensionless) albedo units by dividing flux CRF by the incident solar irradiance. The weakest SW CRF occurs under partly cloudy conditions for marine single-layer low (trade cumulus) and multilayer clouds (Fig. 2a). The SW CRF distribution is very narrow and peaks between 0.0 and −0.01. As cloud cover increases from partly cloudy to mostly cloudy, the SW CRF distribution broadens, and the frequency of multilayer clouds increases dramatically
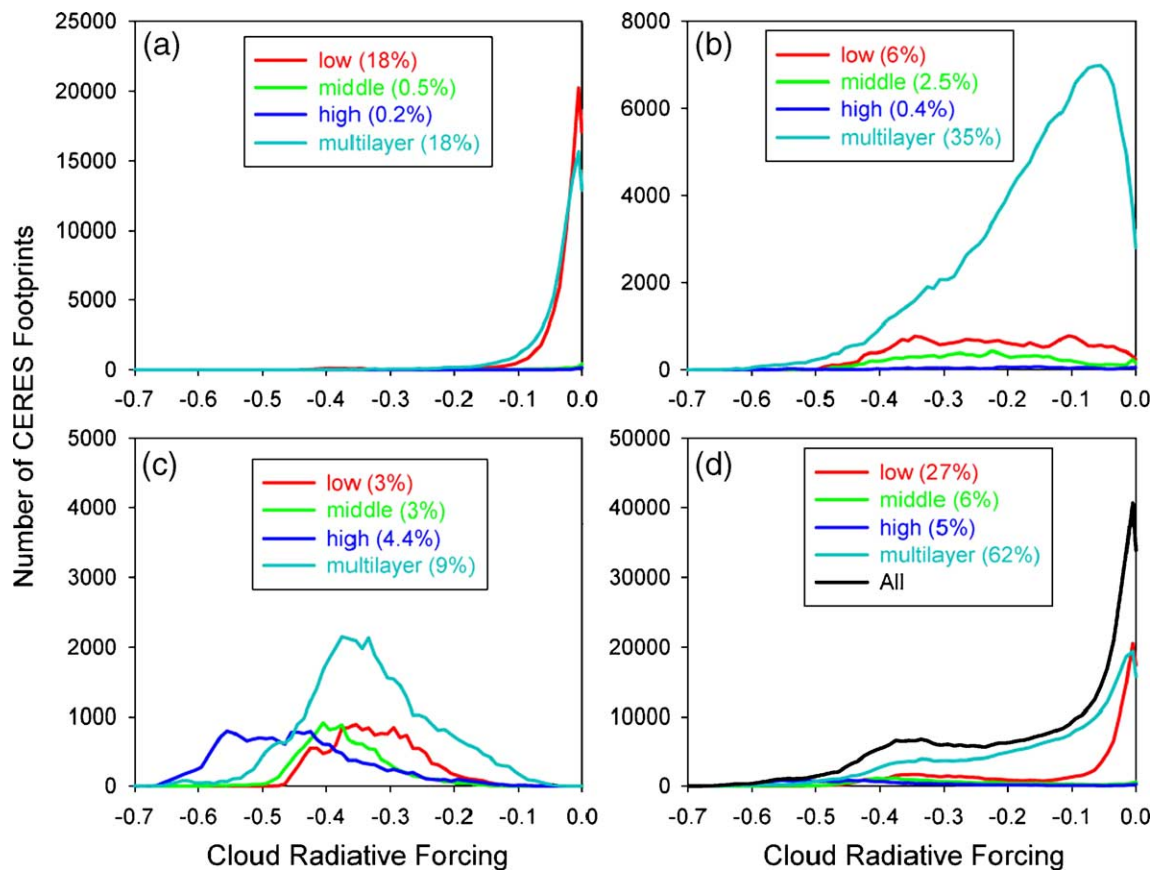

Fig. 2. Frequency distribution of CERES SW CRF for footprints falling in $1° \times 1°$ regions that are (a) partly cloudy, (b) mostly cloudy, (c) overcast, and (d) for all cloud conditions. Numbers in parentheses correspond to the frequency of occurrence of a given cloud class relative to all cloud classes.

(doubles). In $1° \times 1°$ regions that are overcast, SW CRF becomes more pronounced with increasing cloud height, as shown in Fig. 2c. SW radiative cooling for high clouds ranges from approximately -0.15 to -0.65, compared to -0.15 to -0.47 for low clouds.

Because anisotropy is a strong function of spatial resolution, CERES ADMs can only be used to infer CRF at $10–20$ km scales. Furthermore, the relationships between parameters such as cloud liquid water path, optical depth, and albedo are nonlinear, making representations at the typically coarse grid scales of general circulation models problematic. As climate models emerge that are capable of explicitly representing higher-resolution physical and dynamical processes at spatial scales comparable to cloud sizes, the need arises for high-resolution, globally representative observations for testing the models. MISR's high spatial resolution and multiangle capability, in conjunction with CERES broadband multiangle data, provides a uniquely powerful combination that can overcome the resolution limitations of CERES data alone. At scales where individual clouds are resolved, automated stereo image-matching methods make it possible to co-register MISR multiangle radiances at the cloud tops and account for the spatial and angular distribution of radiant energy (Horváth & Davies, 2004; Genkova & Davies, 2003). Cloud type changes rapidly with location, so MISR generates local albedos at 2.2 km resolution, using scene identification and the zenith angle dependence of the observations to constrain modeled radiances in unobserved directions. An example of a stereoscopically derived height field from MISR and the associated narrowband albedo product is shown in Fig. 3. Note that over the short distances (2.2 km) that MISR's local albedo product is generated, values can be greater than 1.0 due to the contributions from the sides of the clouds. CERES measurements in along-track mode provide views coincident with MISR, enabling conversion of high-resolution narrowband MISR albedos to broadband albedos (Davies, 2004).

Reprojection of cloud-leaving radiances to the cloud tops also makes possible automated retrieval of cloud-specific bidirectional reflectance factors (BRFs). BRFs projected to cloud-top altitudes permit direct tests of conventional assumptions invoked when using remotely sensed radiances to infer cloud water content, particularly the reliance on plane parallel (1-D) radiative transfer (RT) theory. Horváth and Davies (2004) show that at MISR's finest resolution the modeled variation of radiance with angle using 1-D RT theory matches the observed variation within $\pm 5\%$ for only about 15% of the global distribution of clouds. This
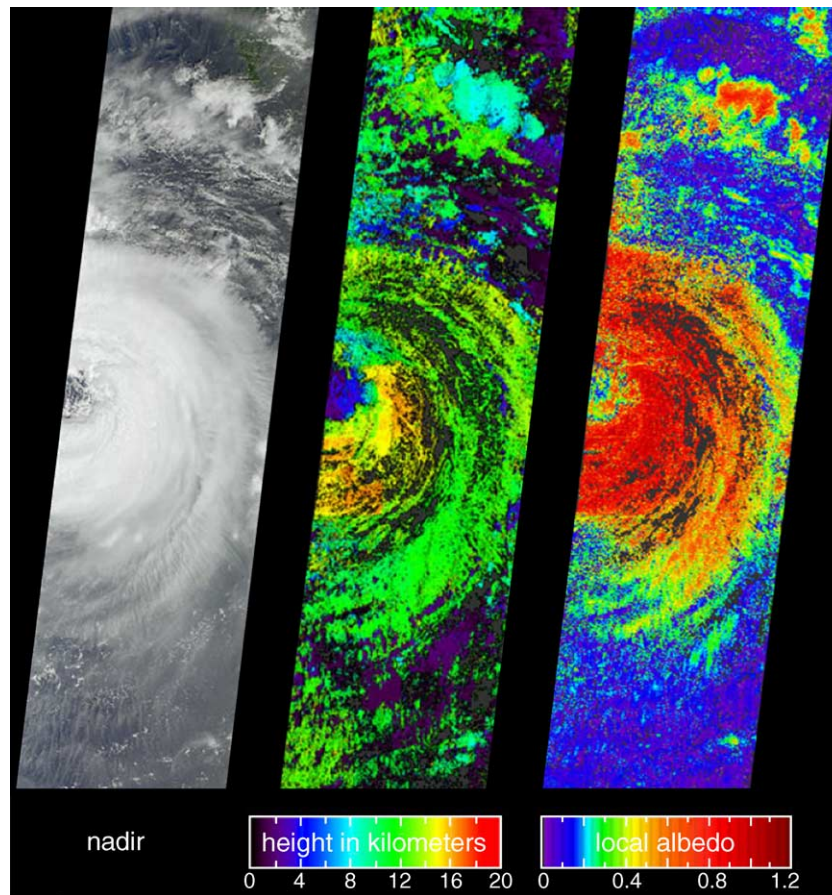

Fig. 3. MISR data from 5 September 2002, when the western portion of Typhoon Sinlaku was situated over the Okinawan island chain. Left: Natural-color nadir view. Center: Cloud-top height field derived using automated stereoscopic processing. Right: Retrieved local albedo. Areas where heights and albedos could not be retrieved are shown in dark gray. These data were acquired during Terra orbit 14442.

percentage rises to about 40% at coarse resolution, albeit for an optical depth that is biased low due to the effects of nonlinear averaging over regions of cloud heterogeneity. Thus, MISR data imply that the use of 3-D RT theory for retrieving cloud optical depths is required for over 60% of Earth's cloud fields. In addition, several studies use MISR data to infer 3-D cloud structure. For example, by observing cloud fraction as a function of angle in MISR data, Kassianov et al. (2003) showed that it is possible to retrieve the geometric thickness of fair-weather cumulus in the tropical Pacific. Zuidema et al. (2003) compared Monte Carlo reflectance simulations of tropical cumulus congestus clouds to MISR BRFs, using the associated stereo height retrievals as constraints on the modeling. In this case, the Monte Carlo simulations did not appear to capture the observed fraction of unobscured sunlit and shadowed cloudy areas, suggesting the presence of radiatively significant cloud variability at scales smaller than the height field resolution of ±550 m. The use of oblique multiangle imagery for the direct reconstruction of cloud 3-D morphologies is now being explored (e.g., Seiz & Davies, submitted for publication). These efforts represent significant steps toward understanding the roles of cloud heterogeneity and vertical structure on passive retrievals of cloud liquid water and associating cloud hydrological characterizations with radiative fluxes.

3.2. Aerosols

3.2.1. Background

Aerosols are liquid or solid airborne particulates having sizes ranging from less than 0.1 μm to more than 1 μm. Most aerosol sources are natural, and include volcanoes, dust storms, forest and grassland fires, living land and oceanic vegetation, and sea spray. Other sources are anthropogenic, such as fossil fuel and biomass burning and ablation from deforested and desertified surfaces. Modeling of the industrial-era temperature record indicates that net aerosol forcing is slightly smaller, but opposite in sign, than forcing from anthropogenic greenhouse gases. However, the uncertainties in aerosol anthropogenic forcing are of the same magnitude as the effects themselves (IPCC, 2001). Calculations of aerosol effects on global climate require the use of chemical transport, radiation, and general circulation models. The validity of these models needs to be evaluated against aerosol information retrieved from satellites and other data sources. Stratification of aerosol optical depths by particle type is a key component of this strategy.

3.2.2. Value of multiangle data

Sensitivity studies indicate that over dark water, multiangle data should be able to separate spherical from randomly oriented non-spherical particles, and make about a dozen distinctions based on particle microphysical properties. These can be mapped to broad, naturally occurring aerosol types: sulfate aerosols, pollution and biomass burning particles, sea salt, and accumulation and coarse-mode dusts (Kahn et al., 1997, 1998, 2001). MISR observations coincident with AErosol RObotic NETwork (AERONET) ground stations (Dubovik et al., 2000; Holben et al., 1998) and with intensive field campaign operations are being used to test aerosol optical depth (Abdou et al., 2004; Diner et al., 2001; Kahn et al., 2005; Martonchik et al., 2004) as well as particle property sensitivity predictions. Although detailed field validation opportunities are rare, on 9 July 2002, as part of the CRYSTAL-FACE campaign, MISR imaged a thin cirrus cloud in the Caribbean Sea just east of the Yucatan Peninsula, while instruments aboard the NASA ER-2 aircraft observed the cloud remotely and the WB-57 aircraft made in situ measurements of the cloud and ambient aerosols. A research aerosol retrieval code (Kahn et al., 2001) applied to MISR data obtained an aerosol optical depth of 0.20, and identified three components: cirrus, contributing 35% to the column optical depth, a medium, spherical, non-absorbing, maritime-type particle contributing 50%, and Saharan dust making up the remaining 15%. Subsequent analysis of the sub-orbital CRYSTAL data confirmed the presence of all three components and their proportions to within about ±10% (Kahn et al., 2003).

Aerosol retrievals in the publicly available MISR products make use of a prescribed set of aerosol models considered to be representative of the types to be found over the globe. The algorithms determine for which models, and at what optical depth for each model, a set of "goodness of fit" criteria is satisfied. Air mass factors ranging from 1 to 3 (owing to the view angle range from nadir to 70°) provide considerable sensitivity to aerosol optical depth, especially for thin haze. MISR's nine near-simultaneous views also cover a broad range of scattering angles, between about 60° and 160° in mid-latitudes, making it possible to constrain aerosol shape and, coupled with the multispectral information, size distribution.

Over deep water bodies, the MISR standard aerosol retrieval algorithm uses the 672 and 866 nm channels (Diner et al., 1999; Martonchik et al., 1998), similar to other sensors that take advantage of the practically negligible surface reflectance at these wavelengths. At high optical depths, data from the 446 and 558 nm bands are also incorporated in the retrieval algorithm, since in such cases, the advantage of having additional spectral information outweighs any contribution from uncertainty in the short-wavelength reflectivity of the ocean surface. One advantage of multiangle observations is that aerosol retrievals over water are possible even when some cameras are affected by sunglint.

Over land, satellite aerosol retrievals are complicated by the large spatial variability in surface bidirectional reflectance, and for much of the Earth the ground reflectance is high, e.g., desert and urban areas, which are major aerosol source regions. The principal problem is separating the surface and atmospheric contributions to the observed top-of-atmosphere radiances. MISR, ATSR-2, and AATSR

make explicit use of multiangle observations to overcome these challenges, as the ratio of atmospheric to surface contributions to the TOA signal increases systematically between the nadir and steeper-angle views. The MISR algorithm models the shape of the surface bidirectional reflectance as a linear sum of angular empirical orthogonal functions derived directly from the image data, making use of spatial contrast and angular variation in the observed signal to separate the surface and atmospheric signals even in situations where bright, dusty aerosols overlay a bright, dusty surface (Diner et al., 2005; Martonchik & Diner, 1992; Martonchik et al., 1998, 2002). A somewhat simpler algorithm, formulated to make use of two look angles, comprises the fundamental aerosol retrieval approach used

by ATSR-2/AATSR (North et al., 1999; Robles González, 2003; Veefkind et al., 1998).

Recent work indicates that MISR can distinguish different dust shape classes (Kalashnikova et al., 2005a, submitted for publication) and cirrus crystal habits (McFarlane et al., in press), the latter complementing MODIS information on cirrus particle size. New dust models were recently incorporated into MISR operational processing to take advantage of this capability (aerosol product version 0016 and higher), and inclusion of a thin cirrus component to the particle models used in MISR retrievals is planned for the future. Other multiangle sensors have also measured features attributable to particle shape. Backscattering anisotropy peaks due to cloud glories and rainbows, and forward
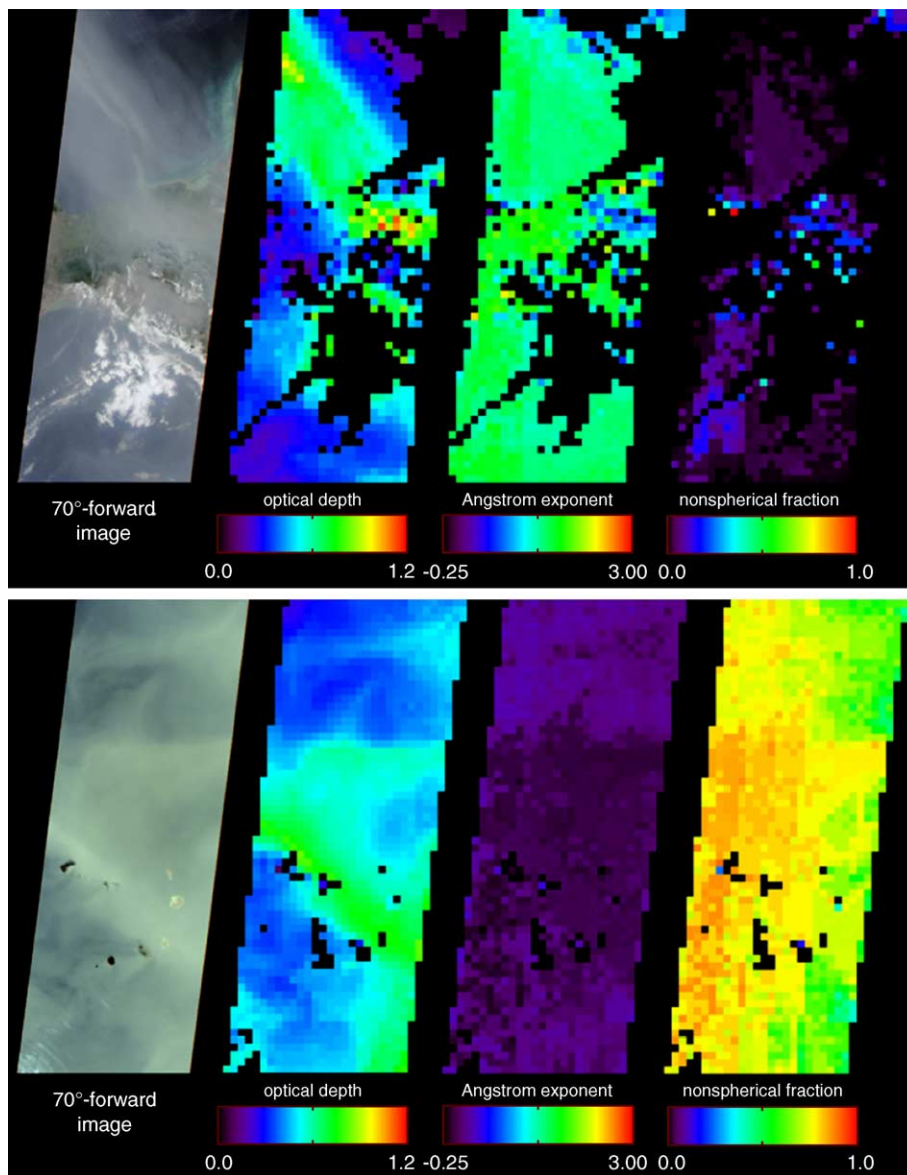

Fig. 4. Top: MISR oblique-camera image and aerosol retrievals over southern Mexico (2 May 2002, Terra orbit 12616), when numerous fires sent smoke drifting northward over the Gulf of Mexico. Bottom: MISR oblique-camera image and aerosol retrievals near the Cape Verde islands, west of Africa and the Sahara desert (6 February 2004, Terra orbit 22006). The width of each image is the full MISR swath—about 400 km across; the vertical dimension is presented at the same spatial scale.

scattering peaks due to specular reflection by horizontally oriented ice crystals have been observed in POLDER (e.g., Chepfer et al., 1999) and CERES data.

Fig. 4 shows example aerosol retrievals from MISR. The top set of data shows a large amount of smoke from fires in southern Mexico, and the bottom set shows Saharan dust blowing over the Cape Verde islands. Each set of panels includes an image from the 70°-forward camera, optical depth at 558 nm, Ångström exponent, and fraction of optical depth due to nonspherical particles. The high Ångström exponent and low nonspherical fraction in the first set, and low Ångström exponent and high nonspherical fraction in the second are consistent with the medium, spherical smoke and large, nonspherical dust expected in these two geographical settings, respectively. Since particle sphericity is more sensitive than optical depth to the selection of scattering angles included in the retrieval, the blockiness in the nonspherical fraction image for the dust storm in Fig. 4 is due to differences in the number of glint-free cameras available for the aerosol retrieval. MISR aerosol retrievals, globally, select component mixtures from the same input aerosol model database, rather than imposing spatially or temporally constrained aerosol types on the retrievals, so within the limits of the database these results demonstrate constraints on aerosol microphysical properties based on the multiangle/multispectral information content of the data. The input models for MISR product versions 0016 and higher consist of 74 mixtures of absorbing and nonabsorbing spherical particles of accumulation and coarse mode distributions in varying proportions, and nonspherical dust. This 74-mixture set replaces a more limited 24-mixture set used with earlier versions of the MISR aerosol product.

MISR generates global monthly and seasonal aerosol optical depth summaries at $0.5° \times 0.5°$ resolution. Fig. 5 shows monthly-averaged aerosol optical depth at 558 nm for March and September 2002. Notable features include retrievals over the bright deserts of North Africa and Saudi Arabia, which are major dust sources, and over snow-covered areas, e.g., Alaska. In the September data, biomass burning aerosols are visible in Southern Africa and South America. High optical depths are found over and downwind of the north African desert and biomass burning source regions, in the southern hemisphere biomass burning regions in September, and near the east Asian population centers, as expected. Low and fairly uniform optical depths appear over the southern oceans. At right are instantaneous MISR/AERONET retrieval matchups for each month. Cases for which the standard deviation of AERONET optical depth within a 2-h window centered on the Terra overpass exceeded 0.05 in the green band are considered indicative of
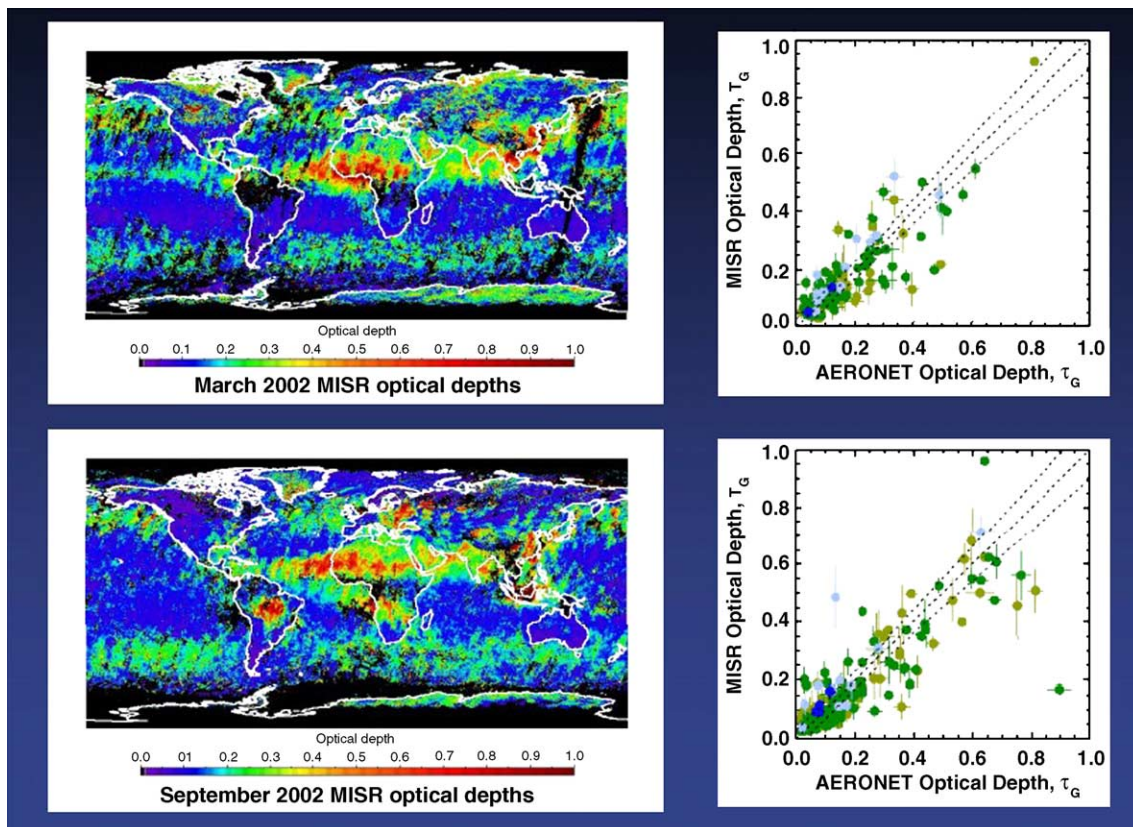

Fig. 5. MISR globally gridded aerosol optical depths (558 nm) for March 2002 (top) and September 2002 (bottom) highlight dust, biomass burning, and pollution sources over Africa, S. America, and Asia. Some cloud masking issues occur at high latitudes. In the right panels, dark blue and green correspond to successful MISR retrieval results for water and land, respectively, within the 17.6-km region containing AERONET sites. If no successful retrieval was obtained, the average result for the surrounding 3×3 array of 17.6-km regions is computed and plotted as light blue or light green.

high aerosol or cloud variability and are excluded from the plots. Each MISR value corresponds to the mean optical depth for all aerosol mixtures in the algorithm climatology that were deemed consistent with the observed radiances. Globally, MISR optical depths have been validated against AERONET and other sunphotometers over a wide variety of surface types (Abdou et al., 2004; Diner et al., 2001; Kahn et al., 2005; Liu et al., 2004a; Martonchik et al., 2004). Kahn et al. (2005) studied biomass burning, continental, dusty, and maritime aerosols, and found that two-thirds of the 558-nm optical depth retrievals fall within 0.05 or 20% of AERONET values, with about a third of the data within 0.03 or 10%, consistent with other studies. In a study over five desert sites (Martonchik et al., 2004), the RMS difference between MISR and AERONET was found to be 0.07 within 17.6-km regions containing the sunphotometers; when averaging of the 3×3 set of surrounding 17.6-km MISR regions is performed, this difference reduces to 0.05, most likely due to the dominance of random retrieval uncertainties over actual spatial variability. Fig. 5 shows that optical depths are currently biased high over homogeneous ice sheets (southern Greenland and Antarctica), in large measure due to unscreened translucent ground fogs. Additional cloud masks based on angular signatures (Di Girolamo & Wilson, 2003), capitalizing on the cloud discrimination capability illustrated below in Section 3.3, will help rectify this situation and are in the process of being incorporated into the MISR data processing software.

Stereoscopic retrievals of biomass burning or dust plume altitudes, using the same methodology described in Section 3.1, constitute another way in which multiangle data aid our understanding of aerosol climate and environmental impacts. Long-range transport and atmospheric residence times of aerosols are governed, among other factors, by the injection altitude and vertical distribution of the particles. Near source regions, where distinct plume features are present, automated MISR stereo processing has demonstrated the ability to retrieve plume-top altitudes (Diner et al., 2004a). Further from the source, as long as there is sufficient spatial contrast within an airmass such that the stereo image matching algorithm will work, altitudes at the top of aerosol layers are retrievable. Using the UV aerosol index from the Total Ozone Mapping Spectrometer (TOMS) as a proxy for aerosol altitude, Fromm and Servranckx (2003) performed a case study of the Chisholm fire in Alberta (May 2001) and inferred that intense convection injected smoke from this large fire up to stratospheric altitudes. Subsequent analysis of MISR data (Diner et al., 2004b) on smoke located 1200 km from the original source provides direct confirmation that stratospheric injection indeed occurred.

As yet, the global climate significance of long-lifetime smoke has not been quantified systematically (Fromm et al., 2004). Complementarity of high-resolution vertical profiling obtained by the CALIPSO lidar (yet to be launched as of this writing), the two-dimensional spatial coverage of plume heights provided by MISR, and sensitivity to high-altitude

aerosol absorption provided by near-UV instruments (e.g., TOMS and the Ozone Mapping Instrument, OMI), and the coupling of such observations with chemical transport models (CTMs), make it possible to address this question. Accurate column optical depths over land, combined with vertical profile information from lidar or from a CTM, also enable the retrieval of surface fine particulate matter concentration ($PM_{2.5}$), an important parameter for evaluating regional air quality. Liu et al. (2004b) showed that MISR aerosol optical depths remove biases in the GEOS-CHEM transport model, yielding annually averaged $PM_{2.5}$ concentrations derived entirely independently of in situ data yet exhibiting excellent, unbiased agreement (slope=1.0, intercept negligible) with EPA surface measurements.

3.3. Cryosphere

3.3.1. Background

The Earth's cryosphere is experiencing rapid change. Over the past two decades, northern sea ice summertime extent and concentration have dropped significantly (e.g., Comiso, 2002; Serreze et al., 2003), changing the ratio of first-year to multi-year Arctic ice. Western Arctic sea ice has shown dramatic thinning (Rothrock et al., 1999). In Antarctica, the loss of Larsen Ice Shelf A in 1995 was followed by the collapse of Larsen Ice Shelf B in 2002 and an ensuing increase in upstream glacier velocity (Scambos et al., 2004). Glaciers in most of the world are retreating and thinning (e.g., Oerlemans, 2001). These changes involve a variety of mechanisms, and linkages between surface structure and radiation. Even small decreases in snow albedo, due, for example, to increased snow grain size or melt, can double the amount of absorbed energy (Nolin & Stroeve, 1997; Stroeve et al., 1997), leading to positive temperature-albedo feedbacks. This can produce meltwater percolation or melt-induced fracturing (Scambos et al., 2000; Zwally et al., 2002), resulting in glacier speed-up or ice shelf disintegration. Ice sheets and sea ice are highly susceptible to the impact of clouds on the surface energy budget, with the net effect of shortwave interception and downwelling longwave re-radiation affecting the timing of snowmelt (Pavolonis & Key, 2003; Zhang et al., 1996). A study by Bintanja and van den Broeke (1996) showed that albedo and cloud transmissivity are of equal importance in determining whether clouds have a warming or cooling effect on ice sheet surfaces. As albedo decreases, clouds do not have to be as optically thick in order for cloud radiative forcing (CRF, defined in Section 3.1) to change from a warming to a cooling effect. For sea ice, a change in the prevalence of thin, young ice is significant in that brine rejection during freezing affects the abundance of cold, saline bottom waters. Thermohaline-driven currents are among the most important components of global ocean circulation (Bindoff et al., 2000; Broeker, 1997; Dickson et al., 2002). In sorting out the dominant mechanisms of cryospheric change, distinguishing ice types is necessary for

understanding the interaction between ice formation and melting, climate, and ocean processes. Documenting the relationships between ice sheet albedo and roughness along with the causes of variability, including melt, fracturing, and ablation is needed to improve models of ice sheet response to climate change, and cloud radiative effects must be taken into account.

3.3.2. Value of multiangle data

Although passive/active microwave approaches have been successful in discriminating multi-year from first-year ice (e.g., Cavalieri et al., 1999; Kwok et al., 1992), characterizing young sea ice types–and connecting these ice types to climate-or weather-related events–remain challenging. The extremely high emissivity and generally low albedo of thin, brine-soaked new ice types limits the effectiveness of passive microwave, and coarse resolution also inhibits detailed mapping of ice sub-types. Thinner ice types appear dark in synthetic aperture radar (SAR) because they are more saline and have dielectric properties that prevent radar energy from penetrating the ice surface. Young ice types have overlapping SAR backscatter signatures, and the thinnest ice types are often below the noise floor of spaceborne SAR (Beaven et al., 1994). Classification of sea ice types using surface roughness discerned at optical wavelengths shows great potential for clear discrimination of new and older ice types. Variations in surface character are thought to arise from very distinct temperature, wind, and wave effects during formation, or from the collisional, thickening, and melt processes that occur over time in sea ice, reflected in both the albedo and bidirectional reflectance characteristics of the surface. In a preliminary study by Nolin et al. (2002) over the Beaufort Sea, ice types within areas classified by the National Ice Center (NIC) as first-year ice were distinguishable by MISR but not discernible by the RADARSAT SAR. CERES measurements indicate, moreover, that the top-of-atmosphere albedo of clear-sky sea ice scenes varies significantly; the mean albedo changes from 0.45 to 0.55 at a solar zenith angle of 55° when sea ice type changes (Kato & Loeb, 2005).

Over ice sheets, surface morphology provides a record of the combined effects of snow accumulation, ablation, and ice movement (Herzfeld et al., 1999). An increase in melt area leads to melt pond incursion into previously smooth regions of the ice sheet. Changes in wind erosion and sublimation affect sastrugi and snow dune formations in the dry snow zone and can strongly modify the angular pattern of reflectance (Warren et al., 1998). Structures such as glacier crevasses and ice surges provide a record of ice dynamics. For example, using multiangle MISR imagery, Landsat, and synthetic aperture radar data, Fricker et al. (2005) discovered a seasonal variation in rift growth rates on the Amery Ice Shelf in East Antarctica, challenging conventional wisdom that the calving of large tabular icebergs is insensitive to seasonal effects. They concluded that ice mélange–a complex, seasonally variable mixture of

sea ice, snow, and ice shelf fragments–and/or seasonal changes in ocean circulation beneath the ice shelf are the most likely explanations for this behavior. In another Antarctic study, Nolin et al. (2002) used MISR data to characterize "blue ice" surfaces on the basis of their surface roughness. These regions of net mass loss are thought to be indicators of changes in ice sheet ablation and accumulation patterns (Bintanja, 1999; Bintanja & Reijmer, 2001; Bintanja & van den Broeke, 1995). Multispectral methods are not able to distinguish them from the spectrally similar crevassed blue ice exposed on active glaciers. However, multiangle MISR data can readily accomplish this distinction based on their textural signatures. Crevassed ice is rough and therefore backward scattering whereas the smooth blue ice (Bintanja et al., 2001) is strongly forward scattering. Future applications might include continent-wide mapping of blue ice areas to examine intra-annual and inter-annual variability within the context of climate change studies.

Nolin et al. (2002) developed a proxy for surface roughness, consisting of a normalized difference angular index (NDAI) that uses a combination of forward and backward scattered radiation. NDAI is defined as (back − fore)/(back + fore), where "back" and "fore" correspond to BRFs at the 60° viewing angles of MISR that happen to be viewing predominantly backward and forward scattering, respectively. NDAI for the area around the Jakobshavn Glacier in western Greenland is illustrated in Fig. 6. The April 2002 NDAI image shows lower values (smoother) along the coast (left side of each image) where the snowpack still covers the rough, non-glacierized terrain. Areas around the main portion of the glacier are also smoother in this image than in the September 2002 image where speckled regions indicate melt ponds that have formed during the melt season. Note that the NDAI values are much greater in September, indicating a significant increase in surface roughness, particularly around the main part of the glacier. There is a much higher degree of variability in NDAI for the upland portion of the glacier drainage basin (center and right portions of the image) in the September image, indicating surface roughness changes induced by changes in surface energy balance.

Satellite observations play a vital role in measuring and monitoring snow and ice albedo at high spatial and temporal resolution with global coverage (e.g., De Abreu et al., 1994; Knap & Oerlemans, 1996; Stroeve et al., 1997). Stroeve and Nolin (2002) found that a linear combination of angular and spectral data from MISR produced improved albedo retrievals compared with a spectral-only model, using regression coefficients derived through comparisons with in situ albedo measurements from several automatic weather stations (AWS) in Greenland. Fig. 7 (top) shows a scatter plot comparing surface albedo at four AWS sites in Greenland with values derived from MISR. The four stations form an elevational transect from the accumulation region to the ablation region of the ice sheet. Overall, the
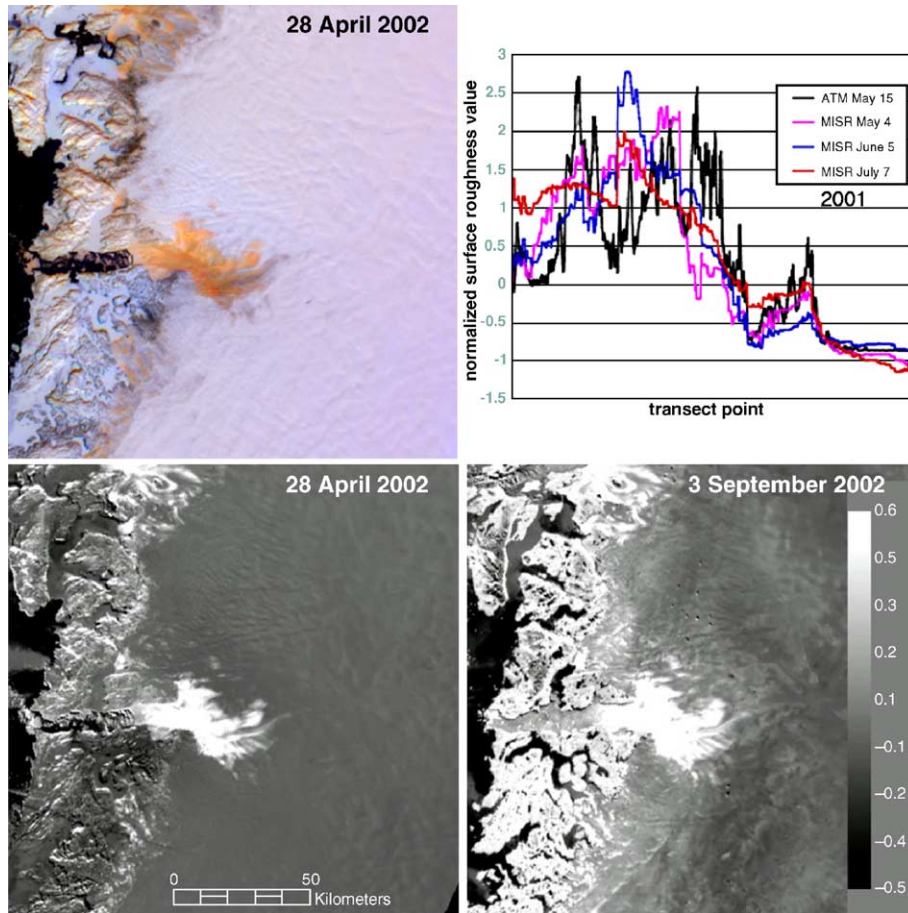
Fig. 6. Upper left: MISR multiangle false color composite of the Jakobshavn glacier, 28 April 2002 (rough areas appear orange, smooth areas appear blue); Bottom left: Normalized difference angular index (NDAI) image from 28 April 2002 (pre-melt); Bottom right: NDAI image from 3 September 2002 (at end of melt season). Brighter NDAI values indicate higher roughness. Upper right: Correlation of relative ice surface roughness derived from MISR (colored lines) and the Airborne Topographic Mapper laser altimeter (black line), for a 2001 transect over the Jakobshavn glacier.

angular-spectral model retrieves a snow surface albedo within about 3% of the in situ measurements, and generates an improved correlation with in situ data relative to a model derived from spectral information alone, particularly at high albedos ($r^2 = 0.89$ for the angular-spectral model vs. 0.82 for the spectral-only model, and the slope is closer to unity when the angular information is included. We also note that the point with the lowest in situ albedo is an outlier for the angular-spectral model. When this point is removed from the regressions, the slope and intercept are 0.97 and 0.02, respectively, for the angular-spectral model and 0.78 and 0.11, respectively, for the spectral-only model). Fig. 7 (bottom) shows the seasonal and spatial variation in surface albedo during the sunlit portion of 2002. Both in situ and satellite measurements show a decrease in surface albedo from April to July as surface temperatures warm, leading to grain growth and eventually, snow melt. As the melt season progresses, surface albedo at each station continues to decline, with large decreases at the JAR1 and JAR2 sites as the snow completely melts, exposing the darker bare glacier ice. By midsummer, an even larger decrease in

surface albedo occurs at JAR1 as compared to JAR2 because dark melt ponds develop around the station and occupy a portion of the satellite ground instantaneous field of view. Surface albedos increase at the end of the sunlit season as new snow begins to blanket the area.

Obtaining an accurate picture of surface radiation budget requires distinguishing clouds from ice and snow and assigning proper heights to polar cloud layers. Comparisons of MISR geometric and MODIS thermal cloud-top heights with ground-based lidar and radar measurements of multi-level clouds show that when optically thin clouds overlay thicker, lower-level clouds, MODIS often detects the higher clouds and assigns an altitude somewhere between the upper- and lower-layer clouds, whereas the MISR operational stereo algorithm detects only the lower clouds. (For computational efficiency, the MISR operational heights are generated from the nadir and near-nadir cameras only; as the oblique cameras are more likely to detect thinner, higher clouds, an ideal approach would be to use all available angles if a computationally efficient approach is developed.) In other cases, if a cloud is close to the surface and in a temperature inversion, cloud-top temperature will be close
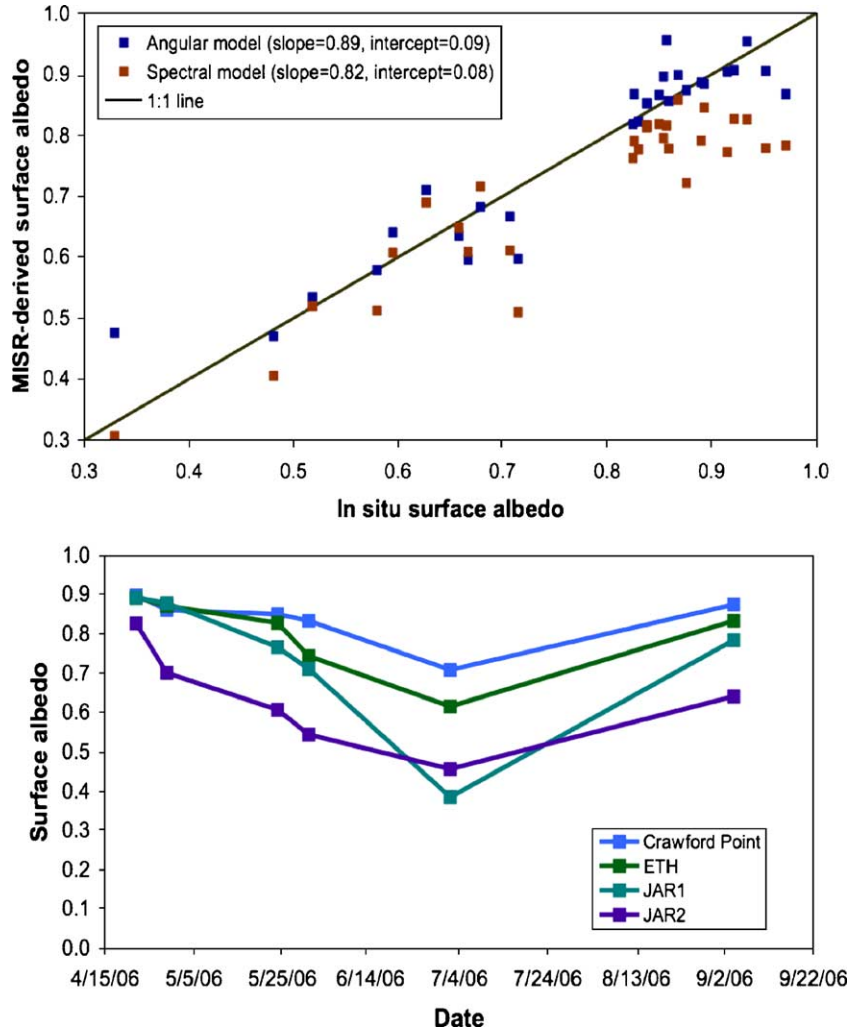
Fig. 7. Top: Comparison between in situ and MISR-derived surface albedo over the Greenland ice sheet, using an angular-spectral regression model (blue) and a spectral-only model (brown). Data from both 2000 and 2001 are shown. The models were developed using 29 MISR images. Bottom: Seasonal variation in broadband albedo at four AWS sites on western margin of the Greenland ice sheet computed using the angular-spectral regression method. Data were acquired during summer 2002. The four AWS sites are Crawford Point (69.88°N/46.97°W, 1958 meters above sea level), ETH (69.57°N/49.29°W, 1148 m.a.s.l.), JAR1 (69.29°N/49.41°W, 967 m.a.s.l.) and JAR2 (69.25°N/50.03°W, 542 m.a.s.l.).

to, or greater than, the surface skin temperature, and multiangle radiance measurements can detect clouds that spectral radiances may not.

The value of multiangle information for polar cloud mapping is illustrated in Fig. 8, where single-band (red) MISR images of the Amery Ice Shelf/Lambert Glacier in Antarctica are combined into a false-color composite: data from the 60° forward-viewing, nadir and 60° backward-viewing cameras are displayed as red, green and blue, respectively. This technique, illustrated in the center panel, uses color as a proxy for angular reflectance variations. Clouds appear purple since they scatter in both the forward and backward directions, making them easily distinguishable from the underlying ice and snow. On the ice surface itself, rough areas exhibit enhanced backward-scattering and appear red/orange (similar to Fig. 6), while smooth areas are predominantly forward-scattering and appear blue. The stereoscopically derived height field shown in the right-

hand panel provides a purely geometric technique for differentiating clouds from ice, and has the simultaneous benefit of providing cloud-top heights.

Analysis of 15 orbits of Terra data over the Arctic Ocean, Greenland, Baffin Bay, and Baffin Island from the daylight season of 2002 shows that the combination of MISR stereo and angular signatures yields a cloud discrimination accuracy of 92% in comparison with expert labels (Shi et al., 2004a). Including MODIS data increases the accuracy to >95% (Shi et al., 2004b). These unprecedented capabilities now make it possible to quantify polar CRF, and research focused on the Arctic–bringing together data from MISR, MODIS, and CERES–is now getting underway. This is timely because during the summers of 2003–2004, MISR data show large decreases in albedo for higher elevations of Greenland (greater than 3σ change compared to previous fluctuations) and of sufficient magnitude to lead to a likely change in the sign of CRF over large portions of the ice
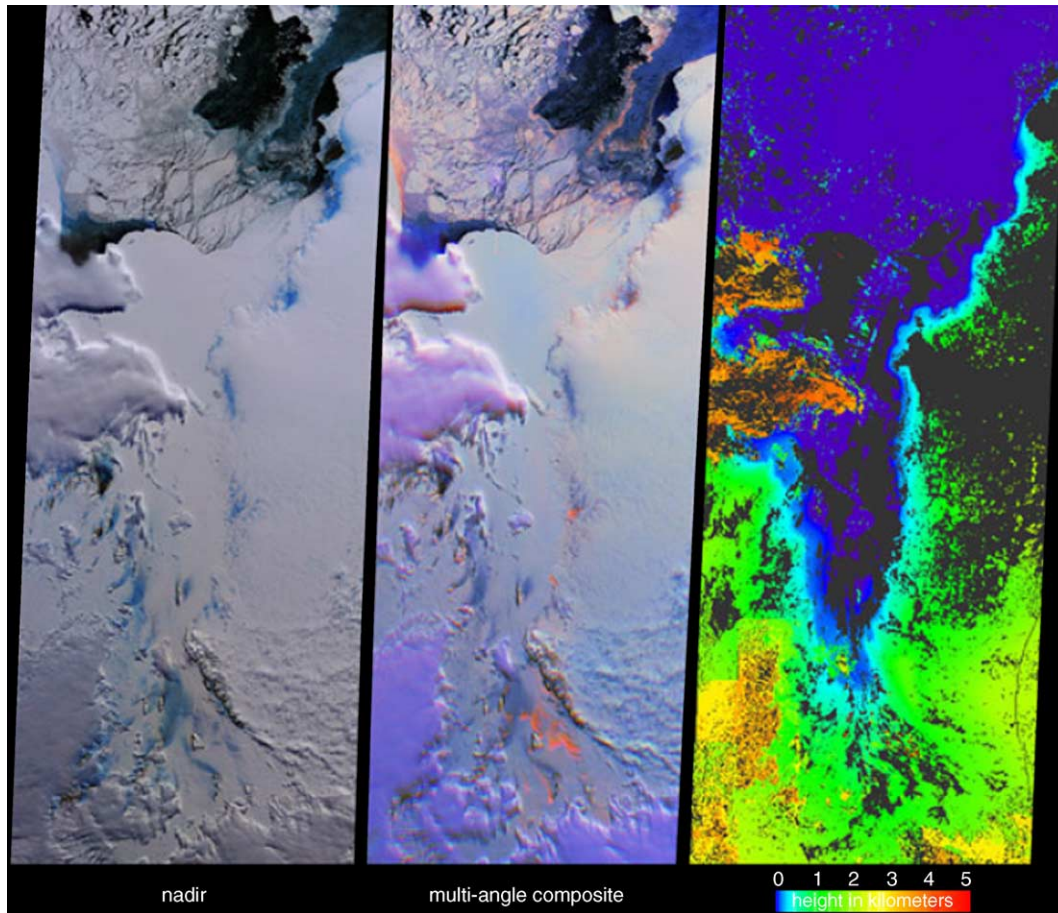
Fig. 8. These views from MISR illustrate ice surface textures, cloud-ice discrimination, and cloud-top heights over the Amery Ice Shelf/Lambert Glacier system in East Antarctica on 25 October 2002 (Terra orbit 15171). Left: Natural-color view from the nadir camera. Center: Multiangular composite in which data from the red band of the 60° forward-viewing, nadir and 60° backward-viewing cameras are displayed as red, green and blue, respectively. Right: Stereoscopically derived height field. Areas exhibiting insufficient spatial contrast for stereoscopic retrieval are shown in dark gray. The small amount of "quilting" over the cloud at lower left in the stereo product is due to imperfect correction for the effect of cloud motion in the automated CTH retrieval.

sheet. The threshold albedo for such a change varies from 0.50 to 0.75 (depending on cloud transmissivity), which is exactly the range of values documented using MISR data for portions of the Greenland ice sheet that in the past 3 years have experienced previously undocumented melt.

3.4. Vegetation

3.4.1. Background

Vegetation structure affects the light-use, water uptake, and nutrient cycling efficiency of canopies, their suitability as wildlife habitats, snow distribution and fresh water availability in forested areas, and fire risk. Changes in vegetation structure over time provide a signature of natural or human disturbances, such as encroachment of woody species into grasslands and savannas and agricultural conversion. Furthermore, vegetation structure determines how solar energy is distributed between the canopy and the ground. Estimates of the green leaf area for the Earth's land surface, called the Leaf Area Index (LAI), and the Fractional amount of Photosynthetically Active Radi-

ation (FPAR) absorbed by the leaves are descriptive of vegetation canopy structure and its energy absorption capacity. Together with surface albedo (Dickinson et al., 1990), these are key state variables in most ecosystem productivity models and in global models of climate, hydrology, and ecology.

3.4.2. Value of multiangle data

The power of multiangle remote sensing for discriminating canopy structural detail has been demonstrated in theoretical studies (e.g. Myneni et al., 1990; Pinty et al., 2002) and field experiments (e.g., Deering et al., 1992). Early proof-of-concept work used multi-overpass (i.e., sequential) Advanced Very High Resolution Radiometer (AVHRR) data to generate approximate BRF patterns of large (>10 kilometer) target areas in the central United States (Privette et al., 1997) and the African Sahel (Braswell et al., 1996). Limitations in the quality of available data underscored the need for datasets designed to provide dense and near-simultaneous observations of vegetation BRF patterns and exploration of combined

multiangle and multispectral sampling for ecological and biogeochemical modeling (Asner et al., 1998). More recently, a number of methods have been investigated to relate surface anisotropy to surface structure (e.g., Chen et al., 2003; Chopping, 2000, Chopping et al., 2002, 2003; Gao et al., 2003; Lacaze et al., 2002; Sandmeier & Deering, 1999; Widlowski et al., 2001).

One of these efforts (Widlowski et al., 2001) uses a parametric approach involving the Rahman-Pinty-Verstraete (RPV) model (Rahman et al., 1993). This model represents a BRF field by three parameters: r_0, an amplitude component that captures the surface brightness; k, an exponent appearing in a modified Minnaert's function (Minnaert, 1941); and Θ, which captures the degree of forward/backward scattering asymmetry, depending on its sign. The k exponent equals 1.0 for a lambertian surface, is <1.0 when a "bowl-shaped" pattern dominates (the spectral BRF values increase with the view zenith angle), and is >1.0 when a "bell-shaped" pattern is observed (the spectral BRF values decrease with the view zenith angle). The angular anisotropy pattern of the solar radiation field scattered by vegetation in the red spectral domain, represented by the k parameter, shows strong potential to reveal surface cover structure at the sub-pixel scale (Pinty et al., 2002).

To explore the relationship between structure and anisotropy, a series of 3-D RT model simulations have been conducted to represent the BRF fields emerging from complex heterogeneous systems as well as their associated canopy height fields. Widlowski et al. (2001, 2004) showed that only the presence of vertically elongated foliage clumps (tree crowns) of medium-to-high densities, overlying a typical soil background, can generate bell-shaped BRF fields. Sparse tree coverage and closed vegetation canopies, on the other hand, have bowl-shaped BRFs. The occurrence of bell-shaped BRFs depends on the relative contribution of the radiation that has traveled through canopy gaps in the both downward and upward directions. For a given Sun position, the amplitude of this so-called uncollided or "black canopy" contribution (i.e., in which the phytoelements are perfectly absorbing) strongly depends on the background reflectance and the structural properties of the canopy, but it always gives rise to a bell-shaped contribution (Pinty et al., 2004). These theoretical results have been corroborated by analyses of data acquired over the Konza prairie in Kansas on 13 July 1999 by the MISR airborne simulator, AirMISR (Pinty et al., 2002). Parametric BRF fitting has also demonstrated a correlation between the k parameter and forest cover density over snow in the Cold Land Processes Experiment (CLPX) study region in Colorado (Nolin, 2004) and in Glacier National Park (Nolin & Selkowitz, 2004). This is significant because forest density affects the surface energy availability for snowmelt and the ability to derive snow-covered area, with ramifications for forest and water resource management.

The predominance of forward over backward scattering, represented by positive values of the RPV Θ parameter, can have diverse causes including the occurrence of a relatively smooth granulated surface (e.g., snow) and/or the presence of liquid surface water. The latter has been used with MISR data to map the impact of dewatering that followed the 26 January 2001 Gujarat earthquake in India (Pinty et al., 2003). Similar analyses have been applied to wetland areas, such as Fig. 9, which displays an RPV Θ map derived from MISR data over Queensland, Australia. It is straightforward to locate the occurrence of free standing water at the surface corresponding to a littoral complex made up of a mosaic of mangroves (Atlas of Australian Resources, 1990).

Other methods for retrieving canopy structural information include 3-D RT-based approaches to BRF inversion, which have demonstrated sensitivity to mean leaf angle inclination (Hu et al., 2003; Myneni & Knyazikhin, 2004), and empirical methods that exploit observed statistical relationships between vegetation canopy properties and combined signatures of multiangle and multispectral reflectance. Capitalizing on the subpixel structural information inherent in MISR data, Braswell et al. (2003) used a neural net to derive accurate fractional-area distributions of primary forest, regrowing forest, and cleared land in a disturbed tropical forest in Para, Brazil, using targeted 30-m resolution Landsat data as the training set. Inclusion of shortwave infrared data from MODIS provided synergistic gains in classification accuracy. Retrieval of land classification parameters from data with ~1 km spatial resolution from MISR and MODIS, taking into account the factor of nine resulting from the multiple angles of MISR, implies about a two order of magnitude reduction in required data volume relative to Landsat, in addition to capabilities for global coverage and more frequent revisits of particular sites. Over the Bartlett experimental forest in New Hampshire, Jenkins et al. (2004) found a high correlation between optical multiangular reflectance signature measured with the MISR airborne simulator, AirMISR, and field observations of stand basal area, with an RMS error of 8 m^2/ha. Extension of this capability to MISR's coarser spatial resolution is the subject of current research. Other studies using neural networks, using lidar canopy height retrievals, imply that moderate resolution multiangle imagery can be "trained" to extend point or profiling measurements to large spatial areas; recent work by Ranson et al. (2005) has demonstrated the potential of this approach using the combination of Laser Vegetation Imaging Sensor (LVIS) and AirMISR, and the combination of Geoscience Laser Altimeter System (GLAS) and MISR, obtaining remarkably good correlation between lidar-derived tree heights and the multiangle reflectance-based predictor.

MISR and MODIS both utilize parametric BRF models to capture surface anisotropy and perform the integrations necessary to produce albedo, and take advantage of the ability to invert such models given adequate cloud-free angular sampling (Kimes et al., 1987; Privette et al., 1996).
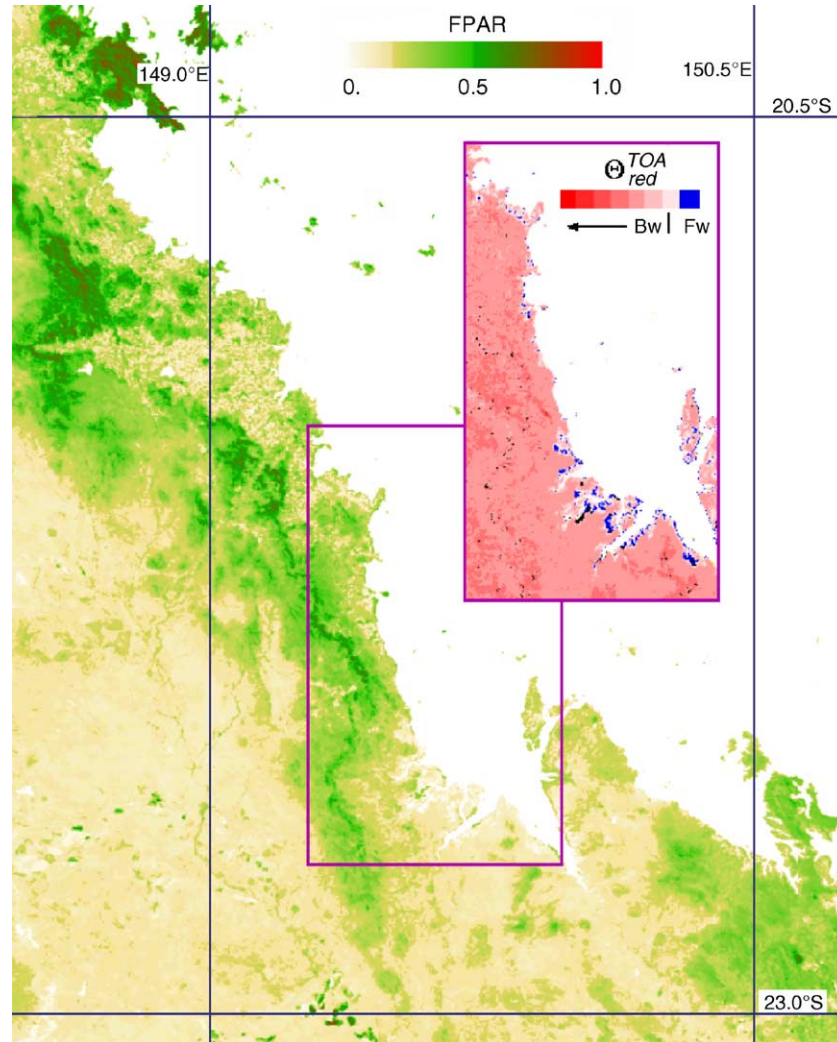
Fig. 9. Map of the RPV Θ parameter value using MISR data from 26 August 2000 over Queensland, Australia (Terra orbit 3679) on top of a surface greenness map generated using the approach of Gobron et al. (2002). The greenness exhibits a large range of variability (low and high FPAR values), which contrasts with a relatively spatially smooth field in the Θ parameter. On top of a spatially smooth background exhibiting preferential backward scattering (shown in red), changes in the dominant scattering regime are illustrated by a sudden increase towards positive values of Θ (shown in blue) along the coastline. These blue spots correspond to a littoral complex made up of a mosaic of mangroves.

For MISR, this is facilitated with a modified form of the RPV model. MODIS employs the RossThick-LiSparse-Reciprocal (RTLSR) model, a semi-empirical linear superposition of two kernels that provide parametric representations of the typical physical patterns of turbid media volumetric scattering and the geometric-optical scattering of sparse vegetation, plus a constant representing isotropic scattering (Lucht et al., 2000; Roujean et al., 1992; Wanner et al., 1997). One application is the production of view angle-adjusted surface reflectances for phenological, land cover classification, or land cover change applications. Various studies have shown that the length of the growing season is changing, which affects the global carbon cycle (Myneni et al., 1997). Using time series of MODIS Nadir BRDF-Adjusted surface Reflectances (NBAR) (Friedl et al., 2002; Zhang et al., 2003) and related products in 2001, coherent spatial patterns of the transition dates of both

greenup onset and dormancy onset were found in northern middle and high latitudes, with vegetation greenup migrating northward about 2 days per latitude degree starting in March and dormancy migrating southward from late September (Zhang et al., 2004a). Urban heat effects in vegetation growth were also demonstrated by the earlier onset of greenup and the later onset of dormancy in urban areas compared to rural areas (Zhang et al., 2004b).

Fig. 10 includes an example of MISR-derived winter and summer seasonal summaries of the directional hemispherical reflectance (DHR), which is a formal representation of albedo defined for illumination conditions at a single incidence angle (i.e., no diffuse skylight, hence the additional name "black-sky albedo"). Noteworthy features include vegetation seasonal changes and the advance and retreat of the snowline. The middle panels are estimates of DHR integrated over the photosynthetically active radiation
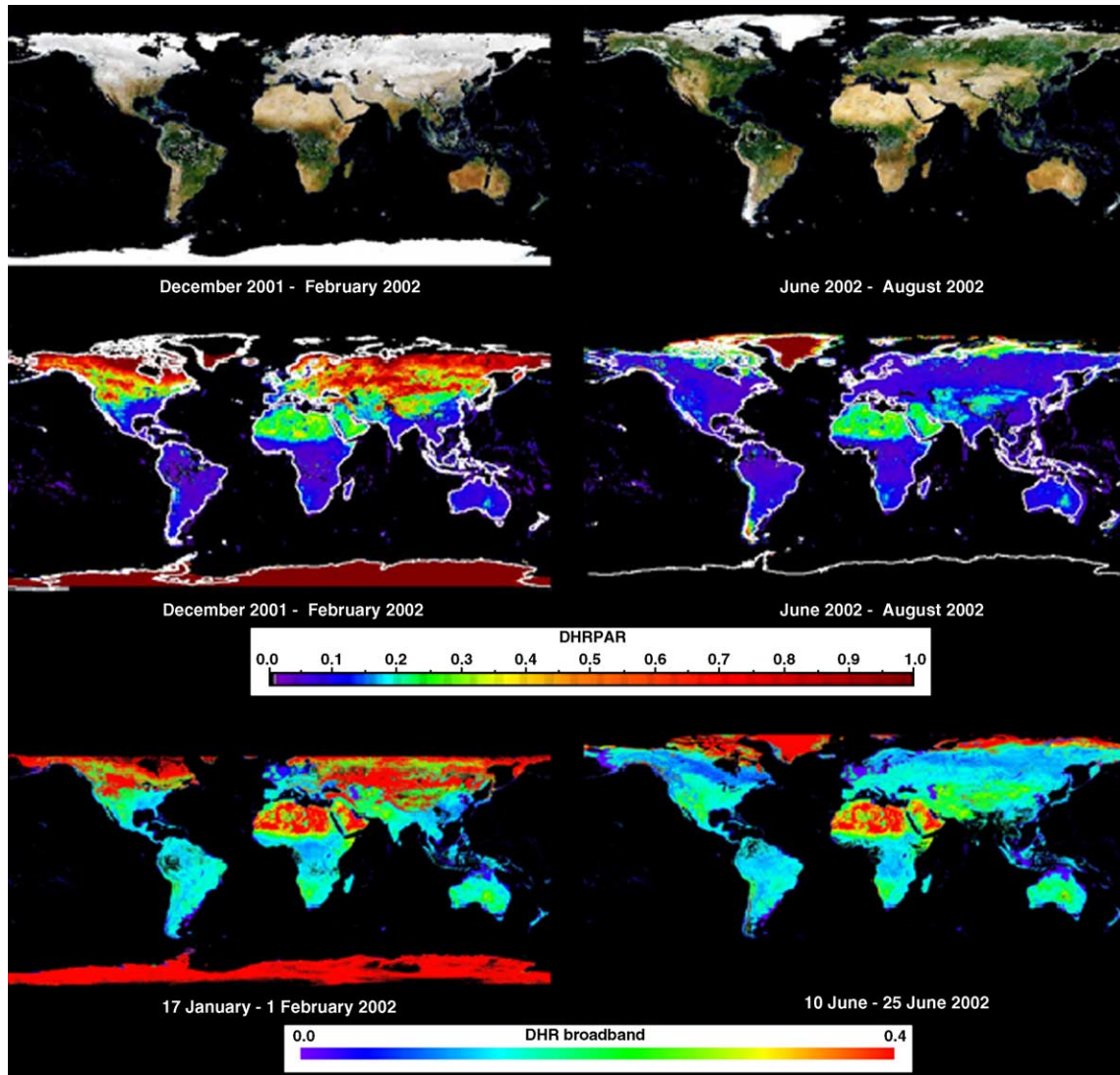
Fig. 10. Top: Global, seasonal summaries of DHR (also called "black-sky albedo") from MISR, at $0.5° \times 0.5°$ spatial resolution. The two image panels show DHR as it was retrieved over land surfaces in MISR's red, green, blue spectral bands for the seasonal periods December 2001–February 2002 (left), and June 2002–August 2002 (right). Middle: Maps of DHR integrated over the photosynthetically active radiation spectral range (400–700 nm), known as DHRPAR, derived from MISR data for the same time periods. Bottom: MODIS broadband ($0.3–5.0$ μm) DHR for the period 17 January–1 February 2002 (left) and for 10 June–25 June 2002 (right). In order to bring out details at albedo <0.4, the MODIS color scale allows albedos >0.4 to saturate, so the MISR and MODIS scales are different.

(PAR) spectral range (400–700 nm) for the same time periods, also derived from the spectral MISR data shown in the top panels. The maps shown at the bottom are the MODIS global total shortwave ($0.3–5.0$ μm) albedos for a single 16-day interval within each seasonal period. Since relatively little sunlight reaches the polar regions during winter, the maps have been cropped to include only the area which is illuminated in both hemispheres during winter and summer. The MODIS algorithm has been shown to successfully capture seasonal and spatial variations of surface anisotropy and albedo globally over a variety of surface covers (Jin et al., 2003a, 2004b; Liang et al., 2002; Roesch et al., 2004; Wang et al., 2004). Case studies show that MODIS and MISR surface bidirectional reflectance factors generally agree in the common spectral bands

(green, red, and near infrared) under similar sun-view geometries (Jin et al., 2002). When narrow-to-broadband conversion factors (Liang, 2001) are applied to the data, comparison of MODIS albedos with independent, instantaneously derived albedos from MISR indicates overall good agreement (Fig. 11). These results enhance our confidence in applying the satellite-retrieved global albedo fields to model intercomparisons. To date, the largest differences between MODIS albedo fields and surface models such as the Community Land Model (CLM2) (Bonan, 1996) show agreement within 5% over snow-free conditions, but have large differences in regions with extensive snow cover, and the model has a large negative bias over the Sahara Desert and the Arabian Peninsula (Oleson et al., 2003; Tsvetsinskaya et al., 2002). Comparisons of MODIS albedo data
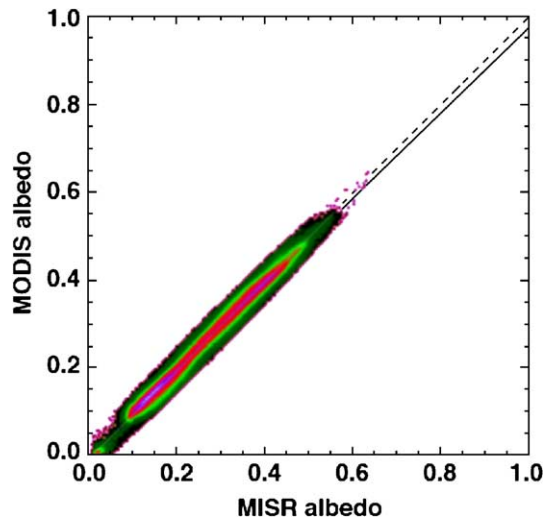
Fig. 11. Estimates of 0.4–1.1 μm land surface albedo for January 2001 using temporal compositing (MODIS) vs. instantaneously-derived values (MISR) (Pinty et al., 2004). Narrow-to-broadband conversion coefficients from Liang (2001) were used.

leaf and stem area indices (Roesch et al., 2004; Zhou et al., 2003).

Global models also need accurate information on how solar energy is distributed between vegetation canopies and the ground. Using the NCAR Community Climate Model, Buermann et al. (2001) reported that satellite-derived LAI reduced the model biases in near-surface air temperature in comparison to observations. A detailed analysis indicated that the use of satellite LAI fields allowed a more realistic partitioning of the incoming solar radiation between the canopy and the underlying ground, resulting in improved model predictions of near-surface climate. This highlights the need for independent estimates of vegetation and ground absorption of solar radiation under various atmospheric conditions to determine the surface energy balance. A principal objective of the MISR multiangular LAI/FPAR algorithm is to retrieve these quantities without requiring a static, pre-specified global biome map. Single angle retrievals, such as with MODIS, require such information to constrain the results, and incorrect information on biome type in such algorithms can fatally impact the LAI/FPAR retrievals (Myneni et al., 2002; Tian et al., 2000). The typical accuracy in most biome maps is about 70% (Lotsch et al., 2003); thus, about 30% of LAI retrievals should be
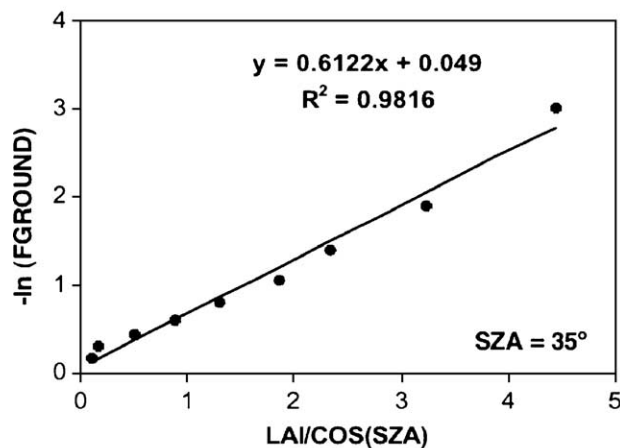
with the Common Land Model and the ECHAM4 global climate model have shown lower model winter albedo in the northern high latitudes, primarily due to overestimation of

Fig. 12. Left: Using MISR Level 2 Land Surface Data over Africa from 23 April 2002 (Terra orbit 12480), the negative logarithm of f_{ground} is plotted against mean LAI normalized to the cosine of the solar zenith angle. The linear relation shows that mean LAI and f_{ground} are related by Beer's law. Right: MISR nadir image of the study area.

treated as unreliable in the case of single-angle data. Performance of the MISR LAI/FPAR algorithm for a limited set of data from Africa suggests that with a probability of about 25%, ambiguities in biome identification were the limiting factor in controlling the LAI uncertainty (Hu et al., 2003). Thus, the joint use of angular and spectral information without a prescribed biome map or training data results in comparable accuracy to LAI values obtained from single-angle retrievals. However, because a pre-defined biome map is not used, the multiangle algorithm can adapt to changing or unknown land cover. Multiangular retrieval of LAI in this manner is analogous to retrievals of aerosol optical depths without pre-specifying the aerosol type or surface spectral reflectance, as discussed in Section 3.2.

The MISR surface product includes PAR-integrated bihemispherical reflectance (BHRPAR), a broadband visible albedo that accounts for both diffuse and direct illumination. From energy conservation, the fraction of PAR absorbed by the ground beneath the canopy is given by the formula $f_{ground} = 1 - BHRPAR - FPAR$. This quantity together with LAI can be used to derive measures of canopy structure for use in ecological models, such as extinction coefficient, which typically is used in conjunction with Beer's law or a two-stream approximation to model radiation. As an additional measure of structure, Fig. 12 uses MISR results to show how the relationship between f_{ground} and LAI depends on mean leaf angle inclination. The term f_{ground} is the downward PAR flux density at the canopy bottom multiplied by the soil absorptance (1-albedo). Since in the photosynthetically active region of the solar spectrum (400–700 nm) leaves usually absorb 85–90% of intercepted radiation, the downward PAR flux density at the canopy bottom can be approximated by the fraction of direct incident PAR that the vegetation canopy transmits. From theoretical expectations, the canopy transmittance (and hence f_{ground}) should be related by Beer's law, given by $\exp[-G(\theta_0)LAI/\cos(\theta_0)]$, where θ_0 is the solar zenith angle (SZA), and $G(\theta_0)$ is a geometric leaf orientation factor defined as the projection of unit leaf area onto a plane perpendicular to the illumination direction (Monsi & Saeki, 1953; Ross, 1981). Using MISR land surface data over Africa from 23 April 2002, Fig. 12 shows that $f_{ground} = 0.95 \cdot \exp[-0.61 \cdot LAI/\cos(\theta_0)]$. According to de Wit's (1965) classification (see also Ross, 1981, pp. 92, 116–117), the value $G(\theta_0) = 0.61$ at SZA=35° corresponds to a canopy with leaves between a planophile (mostly horizontal leaves) and plagophile (mostly leaves at 45°) type of orientation. The coefficient 0.95 depends on the recollision probability (Smolander & Stenberg, 2003, 2005) and the soil albedo (Shabanov et al., 2003; Wang et al., 2003). Multiangular information provides a self-consistent picture of how structure impacts the partitioning of solar energy between a vegetation canopy and the underlying surface.

4. Conclusions

Just as multispectral observations would be of dubious value in a hypothetically gray world, multiangle measurements would have limited utility on a flat, textureless planet. Yet neither of these descriptions pertain to the spatially complex, three-dimensional Earth we inhabit. Single-angle multispectral measurements are powerful, yet incomplete: linking structure and radiation to improve our understanding of the causes and effects of climatic and environmental change demands a multiangular perspective. In this paper, we have illustrated how the synergistic use of multiangle capabilities from the Terra instrument suite provides insights into structure and radiation and the relationships between them. Many of the insights described here could have been realized only through analyses of the unique data products supplied by Terra.

Given the rich content of multiangular imagery, the analyses performed to date have just begun to capitalize on the information provided by this measurement approach. With several years of Terra data now in hand, advances in the use of multiangle data for retrieval of structural information pertaining to clouds, aerosols, and surfaces can be expected with continuing research, and new approaches are already undergoing development and refinement. The upcoming launches of CALIPSO lidar and CloudSat radar will provide unique opportunities for integrating passive retrievals of aerosol and cloud structure with active measurements, particularly at high latitudes where the time difference between these satellites and Terra overpasses are minimized. The cryospheric capabilities described in this paper imply a unique synergy with active and passive microwave systems and with the research themes of the International Polar Year (IPY) (2007–2008). Research activities during IPY intend to determine in detail the present environmental status and to quantify polar environmental change (ICSU, 2004). Over vegetated surfaces radiative transfer modeling experiments (Jacquemoud & Baret, 1990; Verhoef, 1984) reinforce the notion that the spectral and multiangle reflectance data should enable the remote sensing of patterns of vegetation structure and chemistry, and hence productivity. Multiangular measurements of vegetation structure from Terra, along with multispectral and time-series data, are well situated to aid the North American Carbon Program, the implementation phase of which begins in 2005.

Current research efforts are also exploring the utility of hyperspectral multiangle remote sensing (Barnsley et al., 2004), and other activities are looking toward measurement enhancements for the next decade, e.g., global near-ultraviolet and high-accuracy visible/shortwave-infrared polarimetric multiangle imaging of aerosols and clouds at moderately high spatial resolution (Diner et al., 2004c). Fusion of optical multiangle imaging with other techniques, e.g., lidars, radars, and microwave radiometers and

scatterometers offers an exciting vision of future innovations in satellite remote sensing of Earth's atmosphere, cryosphere, and biosphere. The illustrations provided in this paper will hopefully stimulate an even greater involvement of the research community in the application of multiangle data, furthering the use and continued acquisition of such measurements toward improving humankind's understanding and stewardship of our changing planet.

Acknowledgments

References

Abdou, W. A., Diner, D. J., Martonchik, J. V., Bruegge, C. J., Kahn, R. A., Gaitley, B. J., et al. (2004). Comparison of coincident MISR and MODIS aerosol optical depths over land and ocean scenes containing AERONET sites. *Journal of Geophysical Research*, *110*(D10) (Art. No. D10S07).

Abrams, M. (2000). The Advanced Spaceborne Thermal Emission and Reflection Radiometer (ASTER): Data products for the high spatial resolution imager on NASA's Terra platform. *International Journal of Remote Sensing*, *21*, 847–859.

Asner, G. P., Braswell, B. H., Schimel, D. S., & Wessman, C. A. (1998). Ecological research needs from multi-angle remote sensing data. *Remote Sensing of Environment*, *63*, 155–165.

Atlas of Australian Resources. (1990). Volume 6. Commonwealth Government Printer, Canberra, Australia.

Baltsavias, E. (1991). Multiphoto Geometrically Constrained Matching. PhD thesis, Institute of Geodesy and Photogrammetry, ETH Zurich, Switzerland, Mitteilungen Nr. 49.

Barkstrom, B. R. (1984). The Earth Radiation Budget Experiment (ERBE). *Bulletin of the American Meteorological Society*, *65*, 1170–1186.

Barnsley, M. J., Settle, J. J., Cutter, M. A., Lobb, D. R., & Teston, F. (2004). The PROBA/CHRIS mission: A low-cost smallsat for hyperspectral multiangle observations of the earth surface and atmosphere. *IEEE Transactions on Geoscience and Remote Sensing*, *42*, 1512–1520.

Beaven, S. G., Gogineni, S. P., & Shanableh, M. (1994). Radar backscatter signature of thin ice in the central Arctic. *International Journal of Remote Sensing*, *15*, 1149–1154.

Bindoff, N. L., Rintoul, S. R., & Massom, R. A. (2000). Bottom water formation and polynyas in Adélie Land, Antarctica. *Proceedings of the Royal Society of Tasmania*, *133*, 51–56.

Bintanja, R. (1999). On the glaciological, meteorological, and climatological significance of Antarctic blue ice areas. *Reviews of Geophysics*, *37*, 337–359.

Bintanja, R., & Reijmer, C. H. (2001). Meteorological conditions over Antarctic blue-ice areas and their influence on the local surface mass balance. *Journal of Glaciology*, *47*, 37–50.

Bintanja, R., Reijmer, C. H., & Hulscher, S. J. M. H. (2001). Detailed observations of the rippled surface of Antarctic blue-ice areas. *Journal of Glaciology*, *47*, 387–396.

Bintanja, R., & van den Broeke, M. R. (1995). The climate sensitivity of Antarctic blue-ice areas. *Annals of Glaciology*, *21*, 157–161.

Bintanja, R., & van den Broeke, M. R. (1996). The influence of clouds on the radiation budget of ice and snow surfaces in Antarctica and Greenland in summer. *International Journal of Climatology*, *16*, 1281–1296.

Bonan, G. B., (1996). A land surface model (LSM version 1.0) for ecological, hydrological, and atmospheric studies: Technical description and user's guide. NCAR Tech. Note NCAR/TN-417+STR, Natl. Cent. for Atmos. Res., Boulder, CO, 150 pp.

Braswell, B. H., Hagen, S. C., Salas, W. A., & Frolking, S. E. (2003). A multivariable approach for mapping sub-pixel land cover distributions using MISR and MODIS: An application in the Brazilian Amazon. *Remote Sensing of Environment*, *87*, 243–256.

Braswell, B. H., Schimel, D. S., Privette, J. L., Moore III, B., Emery, W. J., Sulzman, E. W., et al. (1996). Extracting ecological and biophysical information from AVHRR optical measurements: An integrated algorithm based on inverse modeling. *Journal of Geophysical Research*, *101*, 23335–23348.

Broeker, W. S. (1997). Thermohaline circulation, the Achilles heel of our climate system: Will man-made CO₂ upset the current balance? *Science*, *278*, 1582–1588.

Buermann, W., Dong, J., Zeng, X., Myneni, R. B., & Dickinson, R. E. (2001). Evaluation of the utility of satellite based vegetation leaf area index data for climate simulations. *Journal of Climate*, *14*(17), 3536–3550.

Cavalieri, D. J., Parkinson, C. L., Gloersen, P., Comiso, J. C., & Zwally, H. J. (1999). Deriving long-term time series of sea ice cover from satellite passive-microwave multisensor data sets. *Journal of Geophysical Research*, *104*, 15803–15814.

Chepfer, H., Brogniez, G. B., Goloub, P., Breon, F. M., & Flamant, P. H. (1999). Observations of horizontally oriented ice crystals in cirrus clouds with POLDER-1/ADEOS-1. *Journal of Quantitative Spectroscopy & Radiative Transfer*, *63*, 521–543.

Chen, J. M., Liu, J., Leblanc, S. G., Lacaze, R., & Roujean, J. -L. (2003). Multi-angular optical remote sensing for assessing vegetation structure and carbon absorption. *Remote Sensing of Environment*, *84*, 516–525.

Chopping, M. J. (2000). Large-scale BRDF retrieval over New Mexico with a multiangular NOAA AVHRR dataset. *Remote Sensing of Environment*, *74*, 163–191.

Chopping, M. J., Rango, A., Havstad, K. M., Schiebe, F. R., Ritchie, J. C., Schmugge, T. J., et al. (2003). Canopy attributes of desert grassland and transition communities derived from multiangular airborne imagery. *Remote Sensing of Environment*, *85*, 339–354.

Chopping, M. J., Rango, A., & Ritchie, J. C. (2002). Improved semi-arid community type differentiation with the NOAA AVHRR via exploitation of the directional signal. *IEEE Transactions on Geoscience and Remote Sensing*, *40*, 1132–1149.

Comiso, J. (2002). A rapidly declining perennial ice cover in the Arctic. *Geophysical Research Letters*, *29*, 1956.

Davies, R. (2004). Spectral-to-broadband albedo and radiance relationships obtained From MISR and CERES measurements. *Proc. fourteenth*

Atmospheric Radiation Measurement (ARM) science team meeting, Albuquerque, NM, March 2004.

Davies, R., & Moroney, C. M. (2005). Proxy measures of 4-year differences in cloud radiative forcing using MISR Data from the Terra satellite. *Eos Transactions AGU, 86.*

De Abreu, R. A., Key, J., Maslanik, J. A., Serreze, M. C., & LeDrew, E. F. (1994). Comparison of in situ and AVHRR-derived surface broadband albedo over Arctic sea ice. *Arctic, 47*, 288–297.

Deering, D. W., Middleton, E. M., Irons, J. R., Blad, B. L., Walter-Shea, E. A., Hays, C. J., et al. (1992). Prairie grassland bidirectional reflectance measured by different instruments at the FIFE site. *Journal of Geophysical Research, 97*, 18887–18903.

Deschamps, P. -Y., Bréon, F.-M., Leroy, M., Podaire, A., Bricaud, A., Buriez, J. -C., et al. (1994). The POLDER mission: Instrument characteristics and scientific objectives. *IEEE Transactions on Geoscience and Remote Sensing, 32*, 598–615.

de Wit, C. T. (1965). Photosynthesis of leaf canopies. *Agricultural Research Reports (Wageningen), 663.*

Dickinson, R. E., Pinty, B., & Verstraete, M. M. (1990). Relating surface albedos in GCM to remotely sensed data. *Agricultural and Forest Meteorology, 52*, 109–131.

Dickson, R. R., Yashayaev, I., Meinke, J., Turrell, W., Dye, S., & Holford, J. (2002). Rapid freshening of the Deep North Atlantic Ocean over the past four decades. *Nature, 416*, 832–837.

Di Girolamo, L., & Wilson, M. (2003). A first look at band-differenced angular signatures for cloud detection from MISR. *IEEE Transactions on Geoscience and Remote Sensing, 41*, 1730–1734.

Diner, D. J., Abdou, W. A., Bruegge, C. J., Conel, J. E., Crean, K. A., Gaitley, B. J., et al. (2001). MISR aerosol optical depth retrievals over southern Africa during the SAFARI-2000 dry season campaign. *Geophysical Research Letters, 28*, 3127–3130.

Diner, D. J., Asner, G. P., Davies, R., Knyazikhin, Y., Muller, J. -P., Nolin, A. W., et al. (1999). New directions in Earth observing: Scientific applications of multiangle remote sensing. *Bulletin of the American Meteorological Society, 80*, 2209–2228.

Diner, D. J., Beckert, J. C., Bothwell, G. W., & Rodriguez, J. I. (2002). Performance of the MISR instrument during its first 20 months in Earth orbit. *IEEE Transactions on Geoscience and Remote Sensing, 40*, 1449–1466.

Diner, D. J., Beckert, J. C., Reilly, T. H., Bruegge, C. J., Conel, J. E., Kahn, R., et al. (1998). Multi-angle Imaging SpectroRadiometer (MISR) description and experiment overview. *IEEE Transactions on Geoscience and Remote Sensing, 36*, 1072–1087.

Diner, D. J., Menzies, R. T., Kahn, R. A., Anderson, T. L., Bösenberg, J., Charlson, R. J., et al. (2004a). Using the PARAGON framework to establish an accurate, consistent, and cohesive long-term aerosol record. *Bulletin of the American Meteorological Society, 85*, 1535–1548.

Diner, D. J., Fromm, M. D., Torres, O., Logan, J. A., Martonchik, J. V., Kahn, R. A., et al. (2004b). New satellite observations of upper tropospheric/lower stratospheric aerosols: Case studies over the U.S. and Canada. *EOS Transactions AGU, 85.*

Diner, D. J., Chipman, R. A., Beaudry, N., Cairns, B., Foo, L. D., Macenka, S. A., et al. (2004c). An integrated multiangle, multispectral, and polarimetric imaging concept for aerosol remote sensing from space. Fourth International Asia-Pacific Environmental Remote Sensing Symposium, Honolulu, HI. *SPIE Proceedings, vol. 5659.*

Diner, D. J., Martonchik, J. V., Kahn, R. A., Pinty, B., Gobron, N., Nelson, D. L., et al. (2005). Using angular and spectral shape similarity constraints to improve MISR aerosol and surface retrievals over land. *Remote Sensing of Environment, 94*, 155–171.

Dubovik, O., Smirnov, A., Holben, B. N., King, M. D., Kaufman, Y. J., Eck, T. F., et al. (2000). Accuracy assessments of aerosol optical properties retrieved from Aerosol Robotic Network (AERONET) Sun and sky radiance measurements. *Journal of Geophysical Research, 105*, 9791–9806.

Fricker, H. A., Young, N. W., Coleman, R., Bassis, J. N., & Minster, B. (2005). Multi-year monitoring of rift propagation on the Amery Ice Shelf, East Antarctica. *Geophysical Research Letters, 32* (Art. No. L02502).

Friedl, M. A., McIver, D. K., Hodges, J. C. F., Zhang, X. Y., Muchoney, D., Strahler, A. H., et al. (2002). Global land cover mapping from MODIS: Algorithms and early results. *Remote Sensing of Environment, 83*, 287–302.

Fromm, M. D., Bevilacqua, R., Stocks, B., & Servranckx, R. (2004). New directions: Eruptive transport to the stratosphere: Add fire-convection to volcanoes. *Atmospheric Environment, 38*, 163–165.

Fromm, M. D., & Servanckx, R. (2003). Transport of fire smoke above the tropopause by supercell convection. *Geophysical Research Letters, 30*, 1542.

Gao, F., Schaaf, C. B., Strahler, A. H., Jin, Y., & Li, X. (2003). Detecting vegetation structure using a kernel-based BRDF model. *Remote Sensing of Environment, 86*, 198–205.

Genkova, I., & Davies, R. (2003). Spatial heterogeneity of reflected radiance from globally distributed clouds. *Geophysical Research Letters, 30.* doi: 10.1029/2003GL018194.

Gobron, N., Pinty, B., Verstraete, M. M., Widlowski, J. -L., & Diner, D. J. (2002). Uniqueness of multiangular measurements: Part 2. Joint retrieval of vegetation structure and photosynthetic activity from MISR. *IEEE Transactions on Geoscience and Remote Sensing, 40*, 1574–1592.

Gruen, A. (1985). Adaptive least squares correlation: A powerful image matching technique. *South African Journal of Photogrammetry, Remote Sensing and Cartography, 14*, 175–187.

Harrison, E. F., Minnis, P., Barkstrom, B. R., Ramanathan, V., Cess, R. D., & Gibson, G. G. (1990). Seasonal variation of cloud radiative forcing derived from the Earth Radiation Budget Experiment. *Journal of Geophysical Research, 95*, 18687–18703.

Hautecoeur, O., & Leroy, M. M. (1998). Surface bidirectional reflectance distribution function observed at global scale by POLDER/ADEOS. *Geophysical Research Letters, 25*, 4197–4200.

Herzfeld, U. C., Mayer, H., Feller, W., & Mimler, M. (1999). Glacier roughness surveys of Jakobshavn Isbrae drainage basin, West Greenland, and morphological characterization. *Zeitschrift für Gletscherkunde und Glazialgeologie, 35*, 117–146.

Holben, B. N., Eck, T. F., Slutsker, I., Tanré, D., Buis, J. P., Setzer, A., et al. (1998). AERONET—A federated instrument network and data archive for aerosol characterization. *Remote Sensing of Environment, 66*, 1–16.

Horváth, Á., & Davies, R. (2001). Simultaneous retrieval of cloud motion and height from polar-orbiter multiangle measurements. *Geophysical Research Letters, 28*, 2915.

Horváth, Á., & Davies, R. (2004). Anisotropy of water cloud reflectance: A comparison of measurements and 1D theory. *Geophysical Research Letters, 31*, L01102. doi:10.1029/2003GL018386.

Hu, J., Tan, B., Shabanov, N., Crean, K. A., Martonchik, J. V., Diner, D. J., et al. (2003). Performance of the MISR LAI and FPAR algorithm: A case study in Africa. *Remote Sensing of Environment, 88*, 324–340.

ICSU (International Council for Science). (2004). A Framework for the International Polar Year 2007–2008, produced by the ICSU IPY 2007–2008 Planning Group, ISBN 0-930357-61-2 (http://www.ipy.org/concept/framework/framework_short.pdf).

IPCC (Intergovernmental Panel on Climate Change). (2001). In Houghton J. T., et al., (Eds.), *Climate Change 2001.* Cambridge University Press. 878 pp.

Jacquemoud, S., & Baret, F. (1990). PROSPECT: A model of leaf optical properties spectra. *Remote Sensing of Environment, 34*, 75–91.

Jenkins, J., Ollinger, S., Braswell, R., Martin, M., Plourde, L., Smith, M. -L., et al. (2004). Detecting patterns of canopy structure and carbon uptake with multi-angle remote sensing. *Presentation at MISR Science Team Meeting, Pasadena, CA, 9 December.*

Jin, Y., Gao, F., Schaaf, C. B., Li, X., Strahler, A. H., Bruegge, C. J., et al. (2002). Improving MODIS surface BRDF/Albedo retrieval with MISR observations. *IEEE Transactions on Geoscience and Remote Sensing,*

40, 1593–1604.Jin, Y., Schaaf, C. B., Gao, F., Li, X., Strahler, A. H., Lucht, W., et al. (2003a). Consistency of MODIS surface bidirectional reflectance distribution function and albedo retrievals: 1. Algorithm performance. *Journal of Geophysical Research*, *108*, 4158. doi:10.1029/2002JD002803.

Jin, Y., Schaaf, C. B., Woodstock, C. E., Gao, F., Li, X., Strahler, A. H., et al. (2003b). Consistency of MODIS surface bidirectional reflectance distribution function and albedo retrievals: 2. Validation. *Journal of Geophysical Research*, *108*, 4159. doi: 10.1029/2002JD002804.

Kahn, R., Banerjee, P., & McDonald, D. (2001). The sensitivity of multiangle imaging to natural mixtures of aerosols over ocean. *Journal of Geophysical Research*, *106*, 18219–18238.

Kahn, R., Banerjee, P., McDonald, D., & Diner, D. (1998). Sensitivity of multiangle imaging to aerosol optical depth, and to pure-particle size distribution and composition over ocean. *Journal of Geophysical Research*, *103*, 32195–32213.

Kahn, R. A., Gaitley, B. J., Crean, K. A., Diner, D. J., Martonchik, J. V., & Holben, B. (2005). MISR global aerosol optical depth validation based on two years of coincident AERONET observations. *Journal of Geophysical Research*, *110*(D10) (Art. No. D10S04).

Kahn, R., Li, W. -H., McDonald, D., Wilson, M., Di Girolamo, L., Comstock, J., et al. (2003). Thin cirrus properties from space using the MISR multi-angle research aerosol retrieval. *CRYSTAL-FACE workshop, Salt Lake City, UT, February 25–27*.

Kahn, R., West, R., McDonald, D., Rheingans, B., & Mishchenko, M. I. (1997). Sensitivity of multiangle remote sensing observations to aerosol sphericity. *Journal of Geophysical Research*, *102*, 16861–16870.

Kalashnikova, O. V., Kahn, R. A., & Li, W. -H., (submitted for publication). The ability of multi-angle remote sensing observations to identify and distinguish mineral dust types: Part 2. Sensitivity data analysis. *Journal of Geophysical Research*.

Kalashnikova, O. V., Kahn, R., Sokolik, I. N., & Li, W. -H. (2005). The ability of multi-angle remote sensing observations to identify and distinguish mineral dust types: Part 1. Optical models and retrievals of optically thick plumes. *Journal of Geophysical Research*, *110*(D18) (Art. No. D18S14).

Kassianov, E., Ackerman, T., Marchand, R., & Ovtchinnikov, M. (2003). Satellite multiangle cumulus geometry retrieval: Case study. *Journal of Geophysical Research*, *108*. doi: 10.1029/2002JD002350.

Kato, S., & Loeb, N. G. (2005). Top-of-atmosphere shortwave broadband observed radiance and estimated irradiance from Clouds and the Earth's Radiant Energy System (CERES) instruments on Terra over polar regions. *Journal of Geophysical Research*, *110*(D7) (Art. No. D07202).

Kimes, D. S., Sellers, P. J., & Diner, D. J. (1987). Extraction of spectral hemispherical reflectance (albedo) of surfaces from nadir and directional reflectance data. *International Journal of Remote Sensing*, *8*, 1727–1746.

Knap, W. H., & Oerlemans, J. (1996). The surface albedo of the Greenland ice sheet: Satellite-derived and in situ measurements in the Sondre Stromfjord area during the 1991 melt season. *Journal of Glaciology*, *42*, 364–374.

Koelemeijer, R. B. A., Stammes, P., & Watts, P. D. (1998). Comparison of visible calibrations of GOME and ATSR-2. *Remote Sensing of Environment*, *63*, 279–288.

Kwok, R., Rignot, E., Holt, B., & Onstott, R. (1992). Identification of sea ice types in spaceborne synthetic aperture radar data. *Journal of Geophysical Research*, *97*, 2391–2402.

Lacaze, R., Chen, J. M., Roujean, J. -L., & Leblanc, S. G. (2002). Retrieval of vegetation clumping index using hot spot signatures measured by multiangular POLDER instrument. *Remote Sensing of Environment*, *79*, 84–95.

Liang, S. (2001). Narrowband to broadband conversion of land surface albedo. I. Algorithms. *Remote Sensing of Environment*, *76*, 213–238.

Liang, S., Fang, H., Chen, M., Shuey, C. J., Walthall, C., Daughtry, C., et al. (2002). Validating MODIS land surface reflectance and albedo products: Methods and preliminary results. *Remote Sensing of Environment*, *83*, 149–162.

Liang, S., Strahler, A. H., Barnsley, M. J., Borel, C. C., Gerstl, S. A. W., Diner, D. J., et al. (2000). Multiangle remote sensing: Past, present and future. *Remote Sensing Reviews*, *18*, 83–102.

Liu, Y., Park, R. J., Jacob, D. J., Li, Q., Ki,laru, V., & Sarnat, J. A. (2004b). Mapping surface concentrations of fine particulate matter using MISR satellite observations of aerosol optical thickness. *Journal of Geophysical Research*, *109*(D22) (Art. No. D22206).

Liu, Y., Sarnat, J. A., Coull, B. A., Koutrakis, P., & Jacob, D. J. (2004a). Validation of multiangle imaging spectroradiometer (MISR) aerosol optical thickness measurements using aerosol robotic network (AERONET) observations over the contiguous United States. *Journal of Geophysical Research*, *109*(D6) (Art. No. D06205).

Loeb, N. G., Kato, S., Loukachine, K., & Manalo-Smith, N. (2005). Angular distribution models for top-of-atmosphere radiative flux estimation from the Clouds and the Earth's Radiant Energy System instrument on the *Terra* satellite. Part I: Methodology. *Journal of Atmospheric and Oceanic Technology*, *22*, 338–351.

Loeb, N. G., Loukachine, K., Smith, N. M., Wielicki, B. A., & Young, D. F. (2003). Angular distribution models for top-of-atmosphere radiative flux estimation from the clouds and the earth's radiant energy system instrument on the tropical rainfall measuring mission satellite. Part II: Validation. *Journal of Applied Meteorology*, *42*, 1,748–1,769.

Loeb, N. G., Smith, N. M., Kato, S., Miller, W. F., Gupta, S. K., Minnis, P., et al. (2003). Angular distribution models for top-of-atmosphere radiative flux estimation from the clouds and the earth's radiant energy system instrument on the tropical rainfall measuring mission satellite. Part I: Methodology. *Journal of Applied Meteorology*, *42*, 240–265.

Lotsch, A., Tian, Y., Friedl, M. A., & Myneni, R. B. (2003). Land cover mapping in support of LAI and FAPAR retrievals from EOS-MODIS and MISR: Classification methods and sensitivities to errors. *International Journal of Remote Sensing*, *24*, 1997–2016.

Lucht, W., Schaaf, C. B., & Strahler, A. H. (2000). An algorithm for the retrieval of albedo from space using semiempirical BRDF models. *IEEE Transactions on Geoscience and Remote Sensing*, *38*, 977–998.

Martonchik, J. V., Bruegge, C. J., & Strahler, A. H. (2000). A review of reflectance nomenclature used in remote sensing. *Remote Sensing Reviews*, *19*, 9–20.

Martonchik, J. V., & Diner, D. J. (1992). Retrieval of aerosol optical properties from multi-angle satellite imagery. *IEEE Transactions on Geoscience and Remote Sensing*, *30*, 223–230.

Martonchik, J. V., Diner, D. J., Crean, K. A., & Bull, M. A. (2002). Regional aerosol retrieval results from MISR. *IEEE Transactions on Geoscience and Remote Sensing*, *40*, 1520–1531.

Martonchik, J. V., Diner, D. J., Kahn, R., Gaitley, B., & Holben, B. N. (2004). Comparison of MISR and AERONET aerosol optical depths over desert sites. *Geophysical Research Letters*, *31*, L16102. doi: 10.1029/2004GL019807.

Martonchik, J. V., Diner, D. J., Kahn, R., Verstraete, M. M., Pinty, B., Gordon, H. R., et al. (1998). Techniques for the retrieval of aerosol properties over land and ocean using multiangle imaging. *IEEE Transactions on Geoscience and Remote Sensing*, *36*, 1212–1227.

McFarlane, S., Marchand, R. T., & Ackerman, T. P., (in press). Retrieval of cloud phase and crystal habit from MISR and MODIS data. *Journal of Geophysical Research*.

Minnaert, M. (1941). The reciprocity principle in lunar photometry. *Astrophysical Journal*, *93*, 403–410.

Monsi, M., & Saeki, T. (1953). Über den Lichtfaktor in den Pflanzengesellschaften und seine Bedeutung für die Stoffproduktion. *Japanese Journal of Botany*, *14*, 22–52.

Moroney, C., Davies, R., & Muller, J. -P. (2002). Operational retrieval of cloud-top heights using MISR data. *IEEE Transactions on Geoscience and Remote Sensing*, *40*, 1541–1546.

Muller, J. -P., Mandanayake, A., Moroney, C., Davies, R., Diner, D. J., & Paradise, S. (2002). MISR stereoscopic image matchers: Techniques and results. *IEEE Transactions on Geoscience and Remote Sensing*, *40*, 1547–1559.

Myneni, R. B., Asrar, G., & Gerstl, S. A. W. (1990). Radiative transfer in three dimensional leaf canopies. *Transport Theory and Statistical Physics*, *19*, 205–250.

Myneni, R. B., Hoffman, S., Knyazikhin, Y., Privette, J. L., Glassy, J., Tian, Y., et al. (2002). Global products of vegetation leaf area and fraction absorbed PAR from year one of MODIS data. *Remote Sensing of Environment*, *83*, 214–231.

Myneni, R. B., Keeling, C. D., Tucker, C. J., Asrar, G., & Nemani, R. R. (1997). Increased plant growth in the northern high latitudes from 1981 to 1991. *Nature*, *386*, 698–702.

Myneni, R. B. & Knyazikhin, Y., (2004). The promise and reality of multi-angle remote sensing of vegetation, *Presentation at MISR Science Team meeting*, Pasadena, CA.

Naud, C., Muller, J. -P., & Clothiaux, E. E. (2002). Comparison of cloud top heights derived from MISR stereo and MODIS CO_2-slicing. *Geophysical Research Letters*, *29*. doi: 10.1029/2002GL015460.

Naud, C., Muller, J. -P., Haeffelin, M., Morille, Y., & Delaval, A. (2004). Assessment of MISR and MODIS cloud top heights through inter-comparison with a back-scattering lidar at SIRTA. *Geophysical Research Letters*, *31* (Art. No. L04114).

Naud, C., Muller, J. -P., Slack, E. C., Wrench, C. L., & Clothiaux, E. E., (in press). Assessment of the performance of a 3-GHz weather radar for cloud top height retrieval. *Journal of Applied Meteorology*.

Nicodemus, F. E., Richmond, J. C., Hsia, J. J., Ginsberg, I. W., & Limperis, T., (1977). Geometrical Considerations and Nomenclature for Reflectance, NBS Monograph 160, National Bureau of Standards, U.S. Department of Commerce, Washington, DC.

Nolin, A. W. (2004). Towards retrieval of forest cover density over snow with MISR. *Hydrological Processes*, *18*. doi: 10.1002/hyp.5803.

Nolin, A. W., Fetterer, F. M., & Scambos, T. A. (2002). Surface roughness characterizations of sea ice and ice sheets: Case studies with MISR data. *IEEE Transactions on Geoscience and Remote Sensing*, *40*, 1605–1615.

Nolin, A. W., & Selkowitz, D. (2004). Multi-angle/multi-spectral mapping of snow covered area and vegetation density using MISR. *EOS Transactions AGU*, *85*(47) (Fall Meet. Suppl., Abstract C31A-0281).

Nolin, A., & Stroeve, J. (1997). The changing albedo of the Greenland Ice Sheet: Implications for climate change. *Annals of Glaciology*, *25*, 51–57.

North, P. R. J., Briggs, S. A., Plummer, S. E., & Settle, J. J. (1999). Retrieval of land surface bidirectional reflectance and aerosol opacity from ATSR-2 multi-angle imagery. *IEEE Transactions on Geoscience and Remote Sensing*, *37*, 526–537.

Oerlemans, J. (2001). *Glaciers and climate change*. A.A. Balkena Publishers.

Ohring, G., Wielicki, B., Spencer, R., Emery, W., & Datla, R. (eds.), (2004). Satellite instrument calibration for measuring global climate change. Report from the Nov 12–14, 2002 Workshop, NISTIR 7047, Nov. 2003, 119 pp.

Oleson, K. W., Bonan, G. B., Schaaf, C. B., Gao, F., Jin, Y., & Strahler, A. H. (2003). Assessment of global climate model land surface albedo using MODIS data. *Geophysical Research Letters*, *30* (Art. No. 1443).

Pavolonis, M. J., & Key, J. R. (2003). Antarctic cloud radiative forcing at the surface estimated from the AVHRR Polar Pathfinder and ISCCP D1 datasets, 1985–93. *Journal of Applied Meteorology*, *42*, 827–840.

Pinty, B., Gobron, N., Verstraete, M. M., Mélin, F., Widlowski, J. -L., Govaerts, Y., et al. (2003). Observing earthquake-related dewatering using MISR/Terra satellite data. *EOS Transactions American Geophysical Union*, *84*, 37.

Pinty, B., Gobron, N., Widlowski, J. -L., Lavergne, T., & Verstraete, M. M. (2004). Synergy between 1-D and 3-D radiation transfer models to retrieve vegetation canopy properties from remote sensing data. *Journal of Geophysical Research*, *109*, D21205. doi: 10.1029/2004JD005214.

Pinty, B., Widlowski, J. -L., Gobron, N., Verstraete, M. M., & Diner, D. J. (2002). Uniqueness of multiangular measurements: Part 1. An indicator

of subpixel surface heterogeneity from MISR. *IEEE Transactions on Geoscience and Remote Sensing*, *40*, 1560–1573.

Privette, J. L., Eck, T. F., & Deering, D. W. (1997). Estimating spectral albedo and nadir reflectance through inversion of simple BRDF models with AVHRR/MODIS-like data. *Journal of Geophysical Research*, *102*, 29529–29542.

Privette, J. L., Emery, W. J., & Schimel, D. S. (1996). Inversion of a vegetation reflectance model with NOAA AVHRR data. *Remote Sensing of Environment*, *58*, 187–200.

Rahman, H., Pinty, B., & Verstraete, M. M. (1993). Coupled surface-atmosphere reflectance (CSAR) model: 2. Semiempirical surface model usable with NOAA Advanced Very High Resolution Radiometer data. *Journal of Geophysical Research*, *98*, 20791–20801.

Ramanathan, V., Cess, R. D., Harrison, E. F., Minnis, P., Barkstrom, B. R., Ahmad, E., et al. (1989). Cloud-radiative forcing and climate: Results from the earth radiation budget experiment. *Science*, *243*, 57–63.

Ranson, K. J., Sun, G. S., & Kimes, D. S. (2005). Use of Lidar and Multiangle data for estimating forest heights. *Presentation at MISR Science Team Meeting, Pasadena, CA, 9 December*.

Robles González, C., (2003). Retrieval of aerosol properties using ATSR-2 observations and their interpretation. PhD thesis, University of Utrecht, Netherlands.

Roesch, A., Schaaf, C., & Gao, F. (2004). Use of moderate-resolution imaging spectrometer bidirectional reflectance distribution function products to enhance simulated surface albedos. *Journal of Geophysical Research*, *109*, D12105. doi: 10.1029/2004JD004552.

Ross, J. (1981). *The Radiation regime and architecture of plant stands*. The Hague, The Netherlands: Dr. W. Junk Publ.

Rothrock, D. A., Yu, Y., & Maykut, G. A. (1999). Thinning of the arctic sea-ice cover. *Geophysical Research Letters*, *23*, 3469–3472.

Roujean, J. L., Leroy, M., & Deschamps, P. Y. (1992). A bidirectional reflectance model of the earth's surface for the correction of remote-sensing data. *Journal of Geophysical Research*, *97*, 20455–20468.

Sandmeier, S., & Deering, D. W. (1999). Structure analysis and classification of boreal forests using airborne hyperspectral BRDF data from ASAS. *Remote Sensing of Environment*, *69*, 281–295.

Scambos, T. A., Bohlander, J. A., Shuman, C. A., & Skvarca, P. (2004). Glacier acceleration and thinning after ice shelf collapse in the Larsen B embayment, Antarctica. *Geophysical Research Letters*, *31*. doi: 10.1029/2004GL020670.

Scambos, T. A., Hulbe, C., Fahnestock, M., & Bohlander, J. (2000). The link between climate warming and break-up of ice shelves in the Antarctic Peninsula. *Journal of Glaciology*, *46*, 516–530.

Schaaf, C. B., Gao, F., Strahler, A. H., Lucht, W., Li, X., Tsang, T., et al. (2002). First operational BRDF, albedo and nadir reflectance products from MODIS. *Remote Sensing of Environment*, *83*, 135–148.

Seiz, G., (2003). Ground- and satellite-based multi-view determination of 3D cloud geometry. PhD thesis, Institute of Geodesy and Photogrammetry, ETH Zurich, Switzerland. IGP Mitteilungen Nr. 80. Available at http://www.e-collection.ethbib.ethz.ch/cgi-bin/show.pl?type=diss&nr=15172

Seiz, G., & Davies, R. (submitted for publication). Reconstruction of cloud geometry from multi-view satellite images. *Remote Sensing of Environment*.

Seiz, G., Davies, R., & Gruen, A., (submitted for publication). Stereo cloud-top height retrieval with ASTER and MISR, *International Journal of Remote Sensing*.

Serreze, M. C., Maslanik, J., Scambos, T. A., Fetterer, F., Stroeve, J., Knowles, K., et al. (2003). A record minimum Arctic sea ice extent and area in 2002. *Geophysical Research Letters*, *30*, 1110.

Shabanov, N. V., Wang, Y., Buerman, W., Dong, J., Hoffman, S., Smith, G. R., et al. (2003). Effect of foliage spatial heterogeneity in the MODIS LAI and FPAR algorithm over broadleaf forests. *Remote Sensing of Environment*, *85*, 410–423.

Shi, T., Yu, B., Clothiaux, E. E., & Braverman, A., (2004a). Cloud detection over snow and ice based on MISR data. Technical Report

663, Department of Statistics, University of California, Berkeley, CA.

Shi, T., Yu, B., Clothiaux, E. E., & Braverman, A. J. (2004b). Fusing information MISR and MODIS for polar cloud detection. *Proc. 2004 Asilomar Conference on Signals, Systems, and Computers.*

Smolander, S., & Stenberg, P. (2003). A method to account for shoot scale clumping in coniferous canopy reflectance models. *Remote Sensing of Environment, 88*, 363–373.

Smolander, S., & Stenberg, P. (2005). Simple parameterizations of the radiation budget of uniform broadleaved and coniferous canopies. *Remote Sensing of Environment, 94*, 355–363.

Stricker, N. C. M., Hahne, A., Smith, D. L., Delderfield, J., Oliver, M. B., & Edwards, T. (1995). ATSR-2. The evolution in its design from ERS-1 to ERS-2. *ESA Bulletin, 83*, 32–37.

Stroeve, J., Nolin, A., & Steffen, K. (1997). Comparison of AVHRR-derived and in situ surface albedo over the Greenland ice sheet. *Remote Sensing of Environment, 62*, 262–276.

Stroeve, J. C., & Nolin, A. W. (2002). New methods to infer snow albedo from the MISR instrument with applications to the Greenland Ice Sheet. *IEEE Transactions on Geoscience and Remote Sensing, 40*, 1616–1625.

Suttles, J. T., Green, R. N., Minnis, P., Smith, G. L., Staylor, W. F., & Wielicki, B. A., et al. (1988). Angular radiation models for Earth-atmosphere systems, Vol. I—shortwave radiation. Rep. NASA RP-1184, NASA, Washington, D.C.

Suttles, J. T., Green, R. N., Smith, G. L., Wielicki, B. A., Walker, I. J., Taylor, V. R., et al. (1989). Angular radiation models for Earth-atmosphere systems, Vol. II-longwave radiation. Rep. NASA RP-1184, NASA, Washington, D.C.

Tian, Y., Zhang, Y., Knyazikhin, Y., Myneni, R. B., Glassy, J., Dedieu, G., et al. (2000). Prototyping of MODIS LAI and FPAR algorithm with LASUR and LANDSAT data. *IEEE Transactions on Geoscience and Remote Sensing, 38*, 2387–2401.

Tsvetsinskaya, E. A., Schaaf, C. B., Gao, F., Strahler, A. H., Dickinson, R. E., Zeng, X., et al. (2002). Relating MODIS-derived surface albedo to soils and rock types over Northern Africa and the Arabian peninsula. *Geophysical Research Letters, 29*, 1353. doi: 10.1029/2001GL014096.

Veefkind, J. P., de Leeuw, G., & Durkee, P. A. (1998). Retrieval of aerosol optical depth over land using two-angle view satellite radiometry during TARFOX. *Geophysical Research Letters, 25*, 3135–3138.

Verhoef, W. (1984). Light scattering by leaf layers with application to canopy reflectance modeling: The SAIL model. *Remote Sensing of Environment, 16*, 125–141.

Wang, Y., Buermann, W., Stenberg, P., Voipio, P., Smolander, H., Häme, T., et al. (2003). A new parameterization of canopy spectral response to incident solar radiation: Case study with hyperspectral data from pine dominant forest. *Remote Sensing of Environment, 85*, 304–315.

Wang, K., Liu, J., Zhou, X., Sparrow, M., Ma, M., Sun, Z., et al. (2004). Validation of the MODIS global land albedo product using ground measurements in a semidesert region on the Tibetan Plateau. *Journal of Geophysical Research, 109*, D05107. doi: 10.1029/2003JD004229.

Wanner, W., Strahler, A. H., Hu, B., Lewis, P., Muller, J. -P., Li, X., et al. (1997). Global retrieval of bidirectional reflectance and albedo over

land from EOS MODIS and MISR data: Theory and algorithm. *Journal of Geophysical Research, 102*, 17143–17161.

Warren, W. G., Brandt, R. E., & O'Rawe Hinton, P. (1998). Effect of surface roughness on bi-directional reflectance of Antarctic snow. *Journal of Geophysical Research, 103*, 25789–25807.

Widlowski, J. -L., Pinty, B., Gobron, N., Verstraete, M. M., & Davis, A. B. (2001). Characterization of surface heterogeneity detected at the MISR/TERRA subpixel scale. *Geophysical Research Letters, 24*, 4639–4642.

Widlowski, J. -L., Pinty, B., Gobron, N., Verstraete, M. M., Diner, D. J., & Davis, A. B. (2004). Canopy structure parameters derived from multi-angular remote Sensing data for terrestrial carbon studies. *Climatic Change, 67*, 403–415.

Wielicki, B. A., Cess, R. D., King, M. D., Randall, D. A., & Harrison, E. F. (1995). Mission to planet Earth: Role of clouds and radiation in climate. *Bulletin of the American Meteorological Society, 76*, 2125–2152.

Xu, K. -M., Wong, T., Wielicki, B. A., Parker, L., & Eitzen, Z. A., (in press). Statistical analyses of satellite cloud object data from CERES. Part I: Methodology and preliminary results of 1998 El Niño/2000 La Niña, *Journal of Climate.*

Yamaguchi, Y., Kahle, A., Tsu, H., Kawakami, T., & Pniel, M. (1998). Overview of Advanced Spaceborne Thermal Emission and Reflection Radiometer (ASTER). *IEEE Transactions on Geoscience and Remote Sensing, 36*, 1062–1071.

Zhang, X., Friedl, M., Schaaf, C. B., & Strahler, A. H. (2004). Climate controls on vegetation phenological patterns in northern mid- and high latitudes inferred from MODIS data. *Global Change Biology, 10*, 1133–1145.

Zhang, X., Friedl, M. A., Schaaf, C. B., Strahler, A. H., Hodges, J. C. F., Gao, F., et al. (2003). Monitoring vegetation phenology using MODIS. *Remote Sensing of Environment, 84*, 471–475.

Zhang, X., Friedl, M., Schaaf, C. B., Strahler, A. H., & Schneider, A. (2004). The footprint of urban climates on vegetation phenology. *Geophysical Research Letters, 31*, L12209. doi: 10.1029/2004GL020137.

Zhang, T., Stamnes, K., & Bowling, S. A. (1996). Impact of clouds on surface radiative fluxes and snowmelt in the arctic and subarctic. *Journal of Climate, 9*, 2110–2123.

Zhou, L., Dickinson, R. E., Tian, Y., Zeng, X., Dai, Y., Yang, Z., et al. (2003). Comparison of seasonal and spatial variations of albedos from MODIS and Common Land Model, 2003. *Journal of Geophysical Research, 109*(D1) (Art. No. D01103).

Zong, J., Davies, R., Muller, J.-P., & Diner, D. J. (2002). Photogrammetric retrieval of cloud advection and top height from the Multi-angle Imaging SpectroRadiometer (MISR). *Photogrammetric Engineering and Remote Sensing, 68*, 821–829.

Zuidema, P., Davies, R., & Moroney, C. (2003). On the angular radiance closure of tropical cumulus congestus clouds observed by the Multi-angle Imaging Spectroradiometer. *Journal of Geophysical Research, 108*(D20), 4626. doi: 10.1029/2003JD003401.

Zwally, H. J., Abdalati, W., Herring, T., Larson, K., Saba, J., & Steffen, K. (2002). Surface melt-induced acceleration of Greenland ice-sheet flow. *Science, 297*, 218–222.